



Wind turbine wakes on escarpments: A wind-tunnel study

Arslan Salim Dar, Fernando Porté-Agel*

Wind Engineering and Renewable Energy Laboratory (WIRE), École Polytechnique Fédérale de Lausanne (EPFL), 1015, Lausanne, Switzerland



ARTICLE INFO

Article history:

Received 9 June 2021

Received in revised form

17 September 2021

Accepted 19 September 2021

Available online 4 October 2021

Keywords:

Wakes

Topography

Wind energy

Particle-image velocimetry

ABSTRACT

In this study, the wake behind a wind turbine located on an escarpment is investigated using particle-image velocimetry in a wind tunnel. Five different escarpment models are used, which vary in the windward side shape from forward facing steps (FFS) with different curvatures at the leading-edge to sinusoidal ramp shapes with varying slopes. The difference in the base flow (flow without the turbine) resulting from the change in the geometry of the escarpment leads to significant differences in the average and dynamic characteristics of the turbine wake. The relatively high level of turbulence intensity in the base flow induced by the FFS escarpments leads to a faster wake recovery accompanied by higher turbulence kinetic energy, compared with the ramp-shaped ones. The self-similar behavior of the velocity deficit profiles in the far wake is confirmed for all the cases; unlike turbine wakes over flat terrain, the wake growth rate is found to be larger in the vertical direction than in the lateral direction. Meandering of the wake is observed to be higher on the FFS escarpment with an upward wake trajectory, compared to the ramp-shaped one. Finally, an analytical model is assessed to predict the wake velocity deficit of the turbine.

© 2021 The Author(s). Published by Elsevier Ltd. This is an open access article under the CC BY license (<http://creativecommons.org/licenses/by/4.0/>).

1. Introduction

The global wind energy capacity has exceeded 600 GW in the year 2019 [1]. Onshore wind energy, in particular, has experienced a tremendous growth since the dawn of this century, accounting for about 96% of the total installed wind energy capacity. With the new onshore wind energy installations expected to cost less than the cheapest fossil fuel alternatives from 2020 onward [2], it has a vital role to play in our transition from fossil fuel to clean energy sources. Some key contributors to the success of wind energy projects are accurate wind resource assessment, wind farm power prediction and layout optimization. Turbine wakes, characterized by high velocity deficit and enhanced turbulence intensity, are one of the most important turbine-induced flow phenomena responsible for reduced power generation (up to 40% when the wind direction is aligned with the turbine rows/columns in wind farm arrays [3,4]) and enhanced fluctuating loads on the downstream turbines. Developing a thorough understanding of these wakes remains, however, a non-trivial task due to the complex nature of interactions between the wakes, the atmosphere and the underlying

terrain. As wind farms operate in the inherently turbulent atmospheric boundary layer (ABL), characterizing wakes under different atmospheric conditions (thermal stability, turbulence intensity, wind shear and veer), wind farm configurations (size and layout) and surface characteristics (roughness, heterogeneity and topography) is crucial for the improvement of existing power prediction and optimization tools, as well as for ensuring optimal integration of wind energy in the electrical grid.

Wake characteristics of wind turbines and farms sited on flat terrain have been studied in great detail over the last two decades. Earlier works investigating single turbine wakes ranged from uniform inflow velocity [5,6] to accounting for boundary layer effects [7–9] under neutral atmospheric conditions. Further research incorporated atmospheric stability [10–13] and wind veer [14] effects in wake development due to thermal stratification and the Coriolis force. While studying single turbines is important for a fundamental understanding of wake flows, wind farms often comprise of multiple turbines grouped together. Flow characteristics inside and above wind farms, including multiple wake interactions, wind direction effects and the influence of wind farms on local meteorology have been extensively explored under different atmospheric conditions [15–27]. Insights gained from these works led to the development of computationally fast analytical tools for single turbine wakes [10,28–31] and wind farm power predictions [32–34], which are widely used today by wind

* Corresponding author.

E-mail addresses: arslan.dar@epfl.ch (A.S. Dar), fernando.porte-agel@epfl.ch (F. Porté-Agel).

farm developers.

In reality, however, there is a high probability that wind turbines and farms are sited on different topographical features, such as hills, ramps and escarpments. Although the flow speed-up induced by the presence of the topography presents a lucrative incentive, the complex flow characteristics such as varying levels of flow shear, enhanced turbulence generation and hill-induced pressure gradients require a comprehensive understanding of the flow in such terrain. Current literature is rich in studies dealing with flows over complex topography, including analytical solutions [35], experimental [36–39] and numerical [40,41] works. Field measurements of flow over topography have been carried out with great success, such as the benchmark studies of flow around the Askervein Hill [42,43] and the Bolund experiment [44,45]. The study of flow over escarpments was pioneered by Bowen and Lindley [46], who characterized the flow over sharp edged escarpments with varying slopes. Wind turbine wake behavior in such challenging terrains is far from understood and has resulted in overestimation of power output and underestimation of mechanical loads in wind farms sited close to escarpments [47]. Some examples of wind farms potentially affected by flow separation across steep escarpments are given by Rowcraft et al. [48]. In the following, a brief account of recent developments pertaining to wind turbines sited on topography is presented.

Politis et al. [49] used two different Reynolds Averaged Navier Stokes (RANS) solvers to simulate wake effects of wind farms in complex terrain, highlighting challenges in the modeling of such complex flows. In addition, they showed that a linear superposition of terrain and wake effects is insufficient to model wakes in complex terrain. Tian et al. [50] did an experimental investigation of a wind farm sited on a Gaussian hill to assess the interaction between the turbine wakes and the topography. They showed that the presence of the hill affects the power performance of the turbines and also influences the wake of the turbines. Shamsoddin and Porté-Agel [51] performed large-eddy simulation (LES) of a wind farm located on topography and validated the results with the experimental data of Tian et al. [50]. Hyvärinen and Segalini placed wind turbines on periodic sinusoidal hills and reported that topography improves turbine performance [52], and wake interaction with the terrain leads to a faster recovery [53]. Recently, an extensive field campaign in Perdigão, Portugal, which aimed at understanding the flow over a double ridged complex site and its interaction with a turbine wake, was conducted [54,55]. A series of studies using data from the Perdigão campaign look to answer some fundamental questions about wakes in challenging terrains. Menke et al. [56] analyzed the wake of the turbine to determine whether it follows the topography or not. Their results found a dependency on atmospheric stability where the wake followed the terrain in stable conditions, was deflected upward in unstable conditions, whereas no deflection was observed in neutral conditions. Han et al. [57] also found that the wind turbine power performance and wake has significant dependence on the atmospheric stability. Barthelmie and Pryor [58] developed an algorithm to automate the wake identification and characterization over a downstream distance of up to 4.5 rotor diameters. Dar et al. [59] extended the work of Berg et al. [60] to study the wakes under different levels of terrain complexity and turbine locations using large-eddy simulation. They found that wakes remain self-similar in complex terrain, although, for a very short downstream distance due to faster wake recovery and higher turbulence compared to the flat terrain. The faster wake recovery is a commonly observed feature among turbines located in highly complex terrains [49,61,62].

To analytically model the effect of topography on wakes, the most common practice is to superimpose the velocity deficit in a

flat terrain on topography [53,63]. This method, however, only works for hills with gentle slopes and yields inaccurate results for steeper terrains. Recently, Shamsoddin & Porté-Agel [64] proposed a new analytical model for turbine wake development over hills, which accounts for the hill-induced pressure gradients and the modified trajectory of the wake. Barthelmie et al. [65] presented a data set from field measurements across an escarpment located at a coastline. The height of the escarpment, however, was limited to 14 m compared to the hub height of 80 m for the turbines located on the escarpment. Lutz et al. [66] performed detached-eddy simulation of a wind turbine wake in a complex terrain, which can be approximated by an escarpment with a certain slope upstream. A comparison with a wind turbine in flat terrain was carried out to highlight the influence of topography. Qian & Ishihara [67] numerically simulated a turbine sited on an escarpment and showed that the wake development is affected by the ratio between the turbine hub height and the hill height. More recently, Dar & Porté-Agel [68] performed a three-dimensional characterization of the wake behind a turbine sited on two different escarpments using tomographic particle-image velocimetry. They showed that the shape of the escarpment has an influence on the mean, as well as the dynamic characteristics of the wake.

The current work is motivated by the need of a systematic study of wind turbine wakes sited on topography. The choice of escarpments as the topographical feature originates from their common existence in the real world. Coastlines, for instance, have the potential to be very good sites for wind farms, as they can benefit from the high winds coming from the oceans and low costs of onshore wind energy installations. Approximately 80% of the ocean coasts are known to have escarpments of varying heights [69]. In addition, escarpments in an onshore environment are also a common site for wind farms [66,70]. One distinguishing feature of escarpments is the shape of their windward side, which can vary from a steep, forward facing step shape to a sloped ramp shape [66,67,70]. The sensitivity of a turbine wake to changes in the shape of the windward side of an escarpment is not well understood. In the current work, we have developed five escarpment models, varying systematically in the shape of the windward side of the escarpments, where a model wind turbine is placed at a distance of one rotor diameter from the leading edge of the escarpment. The objective is to characterize the differences in the wake flow that arise solely due to the change in the shape of the escarpment. The rest of the article is structured as follows: a description of the wind tunnel, wind turbine model, details of escarpment models and flow measurement setup are provided in section 2; key findings from the study are presented in section 3; finally, a summary and conclusions are given in section 4.

2. Experimental setup

2.1. Wind tunnel

The experiments were carried out in the boundary-layer wind tunnel at the WiRE laboratory of EPFL. The wind tunnel is a closed-loop low-speed one, where a 130 kW fan drives the flow in the test section of dimensions 28 m × 2.56 m × 2 m. A contraction with a 5:1 area ratio is present at the inlet of the test section. A natural boundary layer develops over the surface of the wind tunnel without the use of an external tripping mechanism.

2.2. Wind turbine model

The wind turbine model used in the current study is a three bladed model with a rotor diameter D of 15 cm and a hub height z_h of 12.5 cm. The blade profile has a circular arc shape with 5%

camber and 5% thickness with respect to the chord length. The chord length varies from 12 mm at the blade root to 8.4 mm at the blade tip. The model is specifically designed to have power and thrust coefficients comparable to those of full-scale commercial turbines. The turbine rotor results in an aerodynamic blockage ratio of 0.34%. For more details on the turbine model, the reader is referred to Bastankhah & Porté-Agel [71].

2.3. Escarpment model

Five escarpment models are studied in this work. The models differ in the shape of the windward side of the escarpment. The length of the models is 3 m ($\sim 20D$) and the width is equal to 2.5 m (i.e. covering the width of the tunnel cross-section). The height H of the escarpments is chosen to be equal to the hub height of the turbine model (i.e. 12.5 cm), resulting in a solid blockage ratio of about 6.25%. The wind turbine model is placed one rotor diameter downstream of the leading edge of the models. The escarpments can be sub-divided into two categories: forward-facing step (FFS) models, and models with a ramp shape upstream. A description of the model shapes is given in the following.

Forward-facing steps with:

- sharp corner at the leading edge (labeled 90° Edge)
- 5% radius of curvature with respect to the escarpment height at the leading edge (labeled 5% r/H)
- 10% radius of curvature with respect to the escarpment height at the leading edge (labeled 10% r/H)

The flow separation and turbulence intensity generated by the escarpment are known to be highly sensitive to the shape of the leading edge [47]. It will, therefore, be interesting to see how the turbine wake is affected by adding a radius of curvature as small as 5% with respect to the escarpment height.

The ramp shapes are sinusoidal and defined by the following mathematical expression:

$$z_r(x) = \frac{1}{2}H \left[1 + \cos\left(\frac{\pi x}{2L}\right) \right], \quad (1)$$

where H is the escarpment height and L is the half-length of the ramp. The two ramp models are described by:

- half-length $L = 2H$, leading to a maximum local slope of $\sim 21.5^\circ$ (labeled 21.5° Slope)
- half-length $L = 1.25H$, leading to a maximum local slope of $\sim 33^\circ$ (labeled 33° Slope)

Fig. 1 shows the shapes of the five escarpment models.

2.4. PIV setup

Stereoscopic particle-image velocimetry (S-PIV) is used to obtain high spatial resolution flow measurements. The flow is seeded with olive oil particles with a diameter on the order of 1 μm . The field of view is illuminated by a dual head 425 mJ Nd:YAG laser. Two 16-bit sCMOS cameras (2560×2160 pixels) with 55 mm objectives and mounted on Scheimpflug adapters are used for capturing images. The images are taken at a sampling rate of 10 Hz and mean flow quantities are obtained by averaging over 1000 images. The sampling rate used in this study is not fast enough to resolve the smallest temporal scales, but it is sufficient to provide data for computing Reynolds averaged flow characteristics. Moreover, the PIV system also provides instantaneous information on spatial development of the flow in a two-dimensional plane.

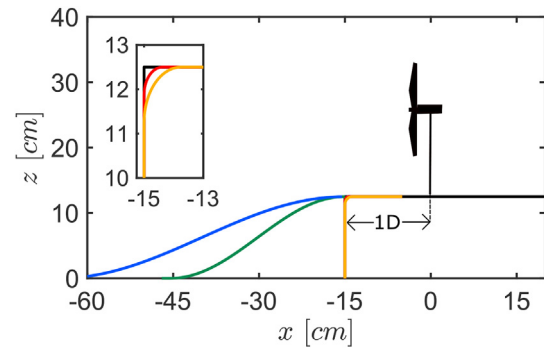


Fig. 1. Side view of the escarpment leading edge for the five topography models. The inset shows a close-up of the leading edge of the forward-facing step models. Black: 90° Edge; red: 5% r/H ; orange: 10% r/H ; green: 33° Slope; blue: 21.5° Slope.

Flow fields in the XZ plane passing through the turbine centerline and YZ planes in the turbine wake are sampled. Fig. 2 shows a schematic representation of the two S-PIV setups. Details of the two setups are given in the following:

- PIV Setup 1: the size of the field of view (FOV) is $4D \times 3D$ with a resolution of 0.0106D. The angle between the cameras is about 45° .
- PIV Setup 2: the size of the field of view (FOV) is $3D \times 2D$ with a resolution of 0.014D. The angle between the cameras is about 42° .

The post-processing is performed in two steps, with an interrogation window size of 64×64 pixels in the first step and 32×32 pixels in the second step. An overlap of 75% is kept within the interrogation windows and the correlation is obtained after two passes through each window size. In addition to the PIV setups described above, a two-dimensional two-component (2D2C) PIV setup using one 16-bit sCMOS camera is used to sample the streamwise and vertical velocity components upstream of the escarpment. The spatial resolution of this PIV setup is also 0.0106D.

3. Results

3.1. Upstream boundary layer and base flow

The upstream boundary layer is characterized using a 2D2C PIV setup. Fig. 3 shows the averaged streamwise velocity U seven rotor diameters upstream of the topography, normalized by the free stream velocity $U_\infty (= 4.37 \text{ ms}^{-1})$ at the same streamwise position. The vertical coordinate $z/D = 0$ in Fig. 3 represents the surface, whereas it represents the center of the turbine on the escarpment in the rest of the article. The boundary-layer height δ is approximately 39 cm and the mean hub height wind speed $U_{h,up}$ is 3.55 ms^{-1} . A power law is fitted to the velocity profile $U = U_{h,up}(z/z_h)^n$, where the scaling exponent n is 0.17. The streamwise turbulence intensity $I_u = \sigma_u/U_\infty$, where σ_u is the standard deviation of the streamwise velocity component, is around 0.06 at the hub height. The normalized vertical momentum flux is higher near the surface due to high shear in that region. A friction velocity u_* of 0.17 ms^{-1} and surface roughness length z_o of 0.04 mm are estimated by fitting a logarithmic profile to the lowest 15% of the boundary layer. The logarithmic fit is done according to the following relation: $U = \frac{u_*}{\kappa} \log\left(\frac{z}{z_o}\right)$, where $\kappa = 0.41$ and the fitted line is shown in Fig. 3 (d). The ratio $z_o/D = 2.67 \times 10^{-4}$ scales to a roughness length of about 0.0267 m for a full-scale turbine of 100 m diameter, corresponding to a terrain with grass and shrubs [72]

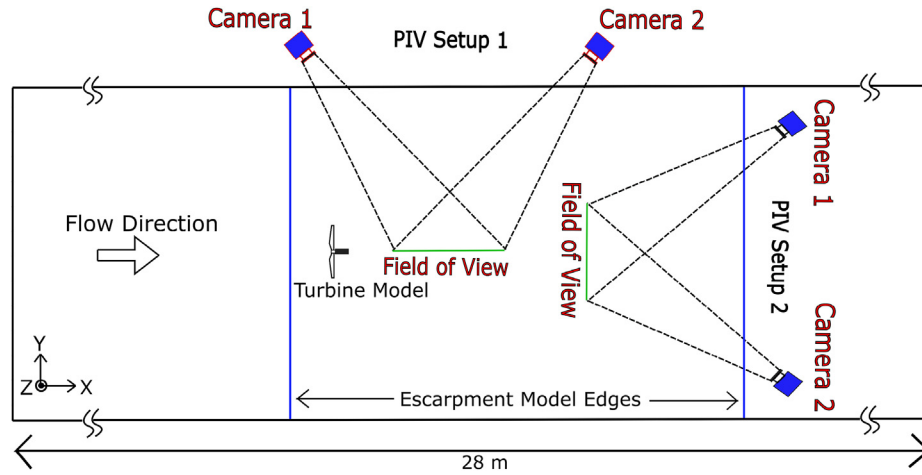


Fig. 2. Schematic representation of the experimental setup and stereoscopic PIV setups (top view).

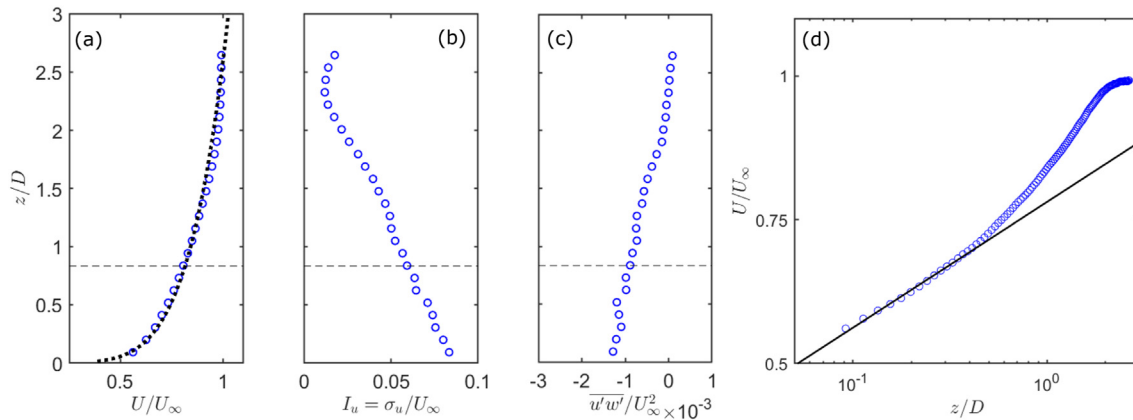


Fig. 3. Vertical profiles of the normalized averaged streamwise velocity component with the power law fit in black dotted line (a), streamwise turbulence intensity (b) and normalized averaged vertical momentum flux (c) in the upstream boundary layer. The horizontal dashed black line shows the height of the escarpment (equal to the hub height). (d) Normalized averaged streamwise velocity in semi-logarithmic coordinates, with the logarithmic fit in black solid line.

upstream of the escarpments. The flow over the escarpments, especially the forward-facing steps, is affected by the ratio of boundary-layer to step height (δ/H) [73]. The δ/H ratio in the current study is 3.12, which is similar to previous experimental studies of flows on escarpments, e.g. see Kilpatrick et al. [74].

The flow characteristics over the escarpments in the absence of the turbine, termed as the base flow, are now discussed. Fig. 4 shows the normalized averaged streamwise component of the flow velocity on the escarpments in the base flow. A separated flow region can be observed in the 90° Edge escarpment case. The reverse flow region is identified by the dark blue contour in the figure. This reverse flow zone has a maximum height of about 0.17 times the escarpment height and the flow reattaches to the surface around two rotor diameters downstream of the leading edge ($x/D = 1$). High flow shear induced by the flow recirculation can be observed. The strength of the flow separation is significantly reduced by just adding a curvature of 5% radius with respect to the escarpment height at the leading edge. The flow reattachment occurs around one rotor diameter from the leading edge. As a result, the shear in the flow is also relatively less in this case. For the forward facing step with a 10% radius of curvature, no recirculation region is observed in the captured field of view. The ramp-shaped escarpments show lesser shear closer to the surface. This is due to the absence of any flow separation, and due to the speed-up of

flow closer to the surface over the escarpment.

An important feature of the flow over escarpments (or, in general, topography) is the flow speed-up across the streamwise transect. This flow speed-up is quantified as the ratio of velocity across the escarpment to a reference velocity in the upstream at the same height relative to the local surface. Fig. 5 shows the speed-up across all the different escarpment models at the hub height. The FFS escarpments have a higher speed-up, with the 90° Edge escarpment showing the highest velocity at the chosen turbine location. The FFS escarpments, however, have a faster decay in the speed-up with the increase in the downstream distance. The escarpments with a ramp upstream have a lower speed-up, but also show a slower decay with the downstream distance compared to the FFS escarpments, which can prove beneficial from the point of view of siting a wind farm on the escarpment.

Table 1 presents some basic flow parameters at the chosen turbine location without the presence of the turbine. The mean streamwise velocity in the base flow at the hub height of the chosen turbine location U_h is used to normalize all the flow quantities in the respective cases. The streamwise turbulence intensity at the hub height is between 0.069 and 0.051 for different cases. It is to be noted that the turbulence intensity in the FFS escarpments is much higher closer to the ground due to high flow shear induced by the flow separation from the escarpment leading edge. The shear

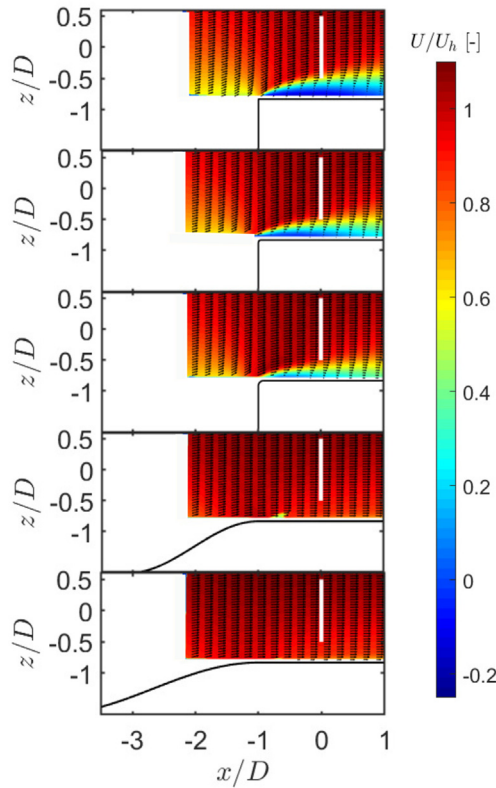


Fig. 4. Contours of the normalized averaged streamwise velocity component without the turbine from top to bottom: 90° Edge, 5% r/H, 10% r/H, 33° Slope and 21.5° Slope. In-plane velocity vectors are overlaid. The prospective turbine rotor is shown by the vertical white line.

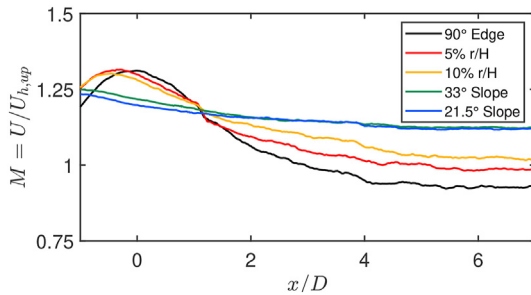


Fig. 5. Flow speed-up across the escarpments (without the turbine). $x/D = 0$ shows the location of the turbine model and $U_{h,up}$ is the streamwise velocity at the hub height in the upstream boundary layer.

Table 1
Overview of key flow parameters at turbine location without the presence of turbine.

	90° Edge	5% r/H	10% r/H	33° Slope	21.5° Slope
U_h (ms^{-1})	4.70	4.60	4.52	4.34	4.27
$I_u = \sigma_u U_h$ (%)	6.9	6.25	6	5.15	5.26
n	0.8171	0.48	0.28	0.12	0.1265

exponents are computed over the rotor diameter as $n = \ln(U_{z_1}/U_{z_2})/\ln(z_1/z_2)$ [65], where z_1 and z_2 are the heights of the rotor top and bottom, respectively. The values of the shear exponents for the FFS escarpments are considerably higher than the recommended value of 0.2 [75] as per IEC standards. This is understandable, as the IEC recommendation is based on turbines

sited on flat terrain. High shear exponents have been observed for escarpments [47,65] and imply high fluctuating loads on the blades. For the ramp-shaped escarpments, the flow shear is reduced compared to the incoming flow due to the effect of flow speed-up closer to the ground.

As per IEC standard 61400-1 edition-3 [75], the inclination angle α with respect to the horizontal axis of the mean flow should be less than 8°. High inclination angles can induce significant additional loads on the rotor. Using the streamwise and vertical velocity components, we compute the flow inclination angles in the absence of the turbine. Very high inclination angles are observed over the leading edge of the FFS escarpments, whereas, ramp-shaped escarpments have inclination angles around 5° (see Fig. 6). At the turbine location, the flow inclination angle ranges from 0° to 6° for the 90° Edge, with a high variation in the lower half of the rotor. The other two FFS cases show very similar trends with α varying between -3° to 3° . The ramp-shaped cases have α less than 3°. It is to be noted that, the inclination angles are within the 8° IEC recommendation for all the escarpment shapes.

3.2. Power and thrust coefficients

The turbine rotor is mounted on a permanent magnet direct current machine. To extract energy from the wind, the DC machine is operated in the ‘generator mode’. The power coefficient C_p is calculated by:

$$C_p = \frac{Q\Omega}{\frac{1}{2}\rho AU_r^3}, \quad (2)$$

where Q is the torque generated by the rotor, Ω the rotational speed, A the rotor area and U_r is the rotor averaged velocity in the base flow at the turbine location. In addition, to measure the thrust force T of the turbine, the tower of the turbine is mounted on a multi-axis strain gauge sensor. The thrust coefficient C_T is calculated by:

$$C_T = \frac{T}{\frac{1}{2}\rho AU_r^2}. \quad (3)$$

Fig. 7 shows the variation of power and thrust coefficients with tip-speed ratio λ for all escarpment models. The maximum power coefficient is between 0.31 and 0.35 for different cases, with the 90° Edge escarpment case showing the maximum C_p out of all the

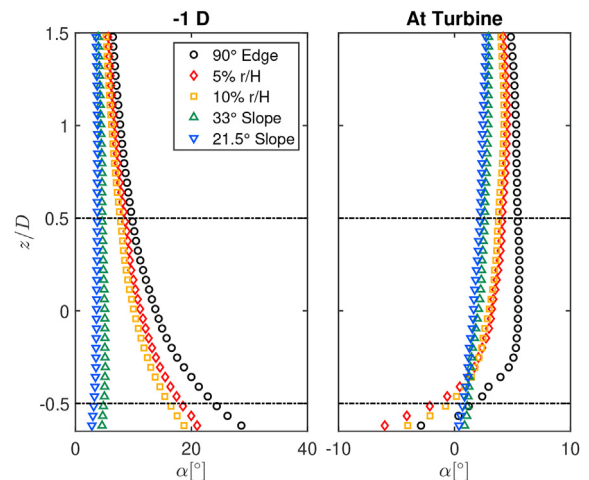


Fig. 6. Flow inclination angle α at the leading edge of the escarpments (-1D) and prospective turbine location. The horizontal lines trace the rotor top and bottom tips.

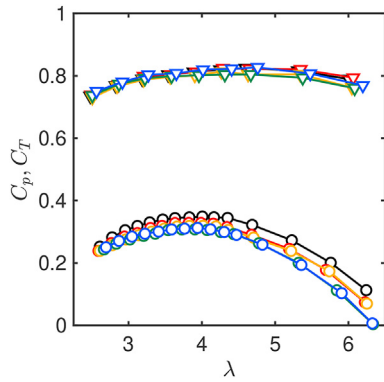


Fig. 7. Power (circles) and thrust (triangles) coefficient as a function of tip-speed ratio for different escarpment models. The colors correspond to same cases as in Fig. 5.

cases. The thrust coefficient is fairly constant between different cases, with an approximate value of 0.8 for the tip speed ratio corresponding to maximum C_p . The tip-speed ratio is adjusted by changing the rotational speed of the rotor while keeping the incoming velocity constant. For PIV measurements, the turbine is operated at the tip-speed ratio corresponding to the maximum C_p for each case.

3.3. Mean flow and turbulence characteristics

We now present some key features of the flow in the wake of the turbine. Fig. 8 shows the averaged normalized streamwise component of the flow velocity. In the FFS escarpments, the recirculation near the surface in the base flow is removed in the presence of the turbine. The normalized streamwise velocity is lowest in the turbine wake for the 90° Edge case, with values getting higher with the increase in the leading edge curvature. The ramp-shaped escarpments show even higher normalized streamwise velocity in the turbine wake. This can be explained by the fact that, as the normalized streamwise velocity in the base flow near the

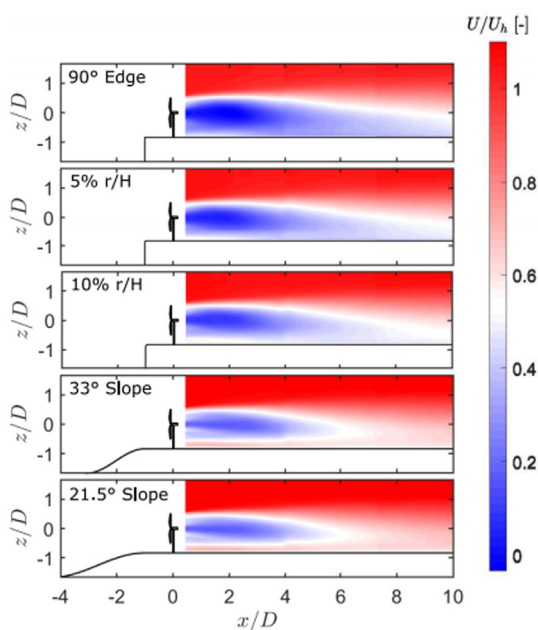


Fig. 8. Contours of the normalized averaged streamwise velocity component in the wake of the turbine for all cases.

surface increases with the increase in the leading edge curvature and with the addition of the ramp, the normalized streamwise velocity in the turbine wake also increases.

The turbulent momentum fluxes play a role in the exchange of energy between the outer and wake flow, thereby contributing to the recovery of the wake. In addition, these fluxes are responsible for the mechanical production of turbulence along with the mean shear in the flow. Figs. 9 and 10 show the normalized vertical and lateral momentum fluxes, respectively, in the turbine wake for different escarpment cases. The magnitude of these fluxes is highest in the 90° Edge case and shows a gradual decrease with the increase in the leading edge curvature. The magnitude of these fluxes gets even smaller with the addition of the ramp in front of the escarpment. An exchange of momentum between the turbine wake and the outer flow near the surface can also be observed in the FFS escarpments at shorter downstream distances from the turbine.

Contours of the normalized turbulence kinetic energy ($tke = \frac{1}{2}(u'^2 + v'^2 + w'^2)$, where u' , v' and w' are the fluctuating part of the streamwise, spanwise and vertical velocity components, respectively) in the turbine wake are shown in Fig. 11. The highest magnitude of the normalized tke is observed in the 90° Edge case, with maximum energy at around 3 rotor diameters downstream. The magnitude of the normalized tke decreases with the increase in the leading edge curvature, and it is almost half for the ramp-shaped cases when compared to the 90° Edge case. In general, the trend observed in the magnitude of the tke with respect to the escarpment shape is consistent with that of the turbulent momentum flux. As explained by Wu & Porté-Agel [77], the flow shear around the rotor bottom tip is small which leads to less turbulence production in this region compared to the rotor top tip, even though the magnitude of the turbulent momentum flux is almost the same in both regions. As a result, the region of high tke resembles a horseshoe shape, whose width is highest for the 90° Edge case and decreases for the curved edged FFS and ramp-shape cases. Another interesting observation is the presence of high turbulence kinetic energy close to the surface surrounding the turbine wake in the FFS escarpment cases. This high tke region is a result of the high shear induced by the flow separation from the escarpment leading edge.

3.4. Wake structure

In order to characterize the difference in the turbine wake flow with respect to the base flow, the streamwise velocity deficit is computed. For this purpose, the streamwise velocity in the base flow is subtracted from that in the wake flow as $\Delta U = U_b - U_w$, where U_b and U_w is the time averaged streamwise velocity in the base and wake flow, respectively. Fig. 12 shows the two dimensional velocity deficit fields in several y-z planes at different downstream distances from the turbine. The presence of the turbine has an impact on the surrounding flow over the FFS escarpments. This is evident from the negative velocity deficit region surrounding the lower part of the rotor up to a downstream distance of 3D in these cases. The magnitude of this negative velocity deficit decreases with the increase in the curvature of the escarpment leading edge. This negative velocity deficit region is generated as the presence of the turbine suppresses the development of separated flow from the escarpment leading edge, which causes a decrease in the mean flow shear in the surrounding flow and higher velocity compared to those in the base flow, thereby leading to a negative velocity deficit region in the FFS escarpments.

The rotation of the wake up to a downstream distance of 3D is also affected by the escarpment geometry. Specifically, the vertical

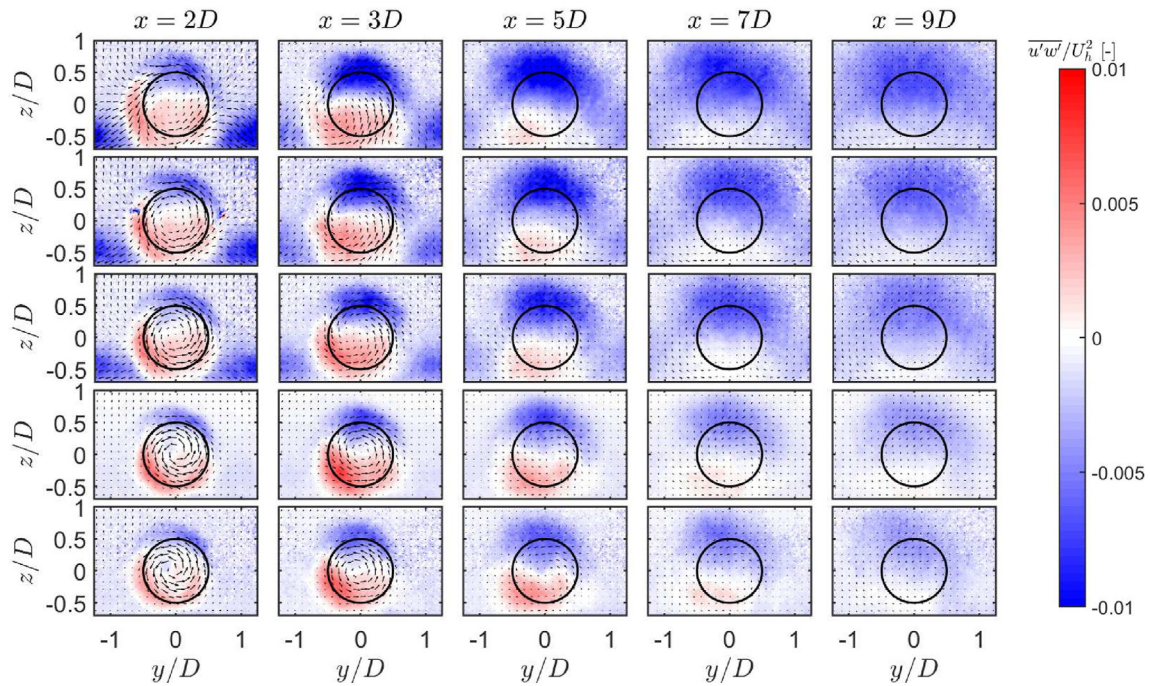


Fig. 9. Contours of the normalized vertical momentum flux in the wake of the turbine. From top to bottom: 90° Edge, 5% r/H, 10% r/H, 33° Slope, 21.5° Slope. In-plane velocity components are overlaid. Black circles represent the rotor position.

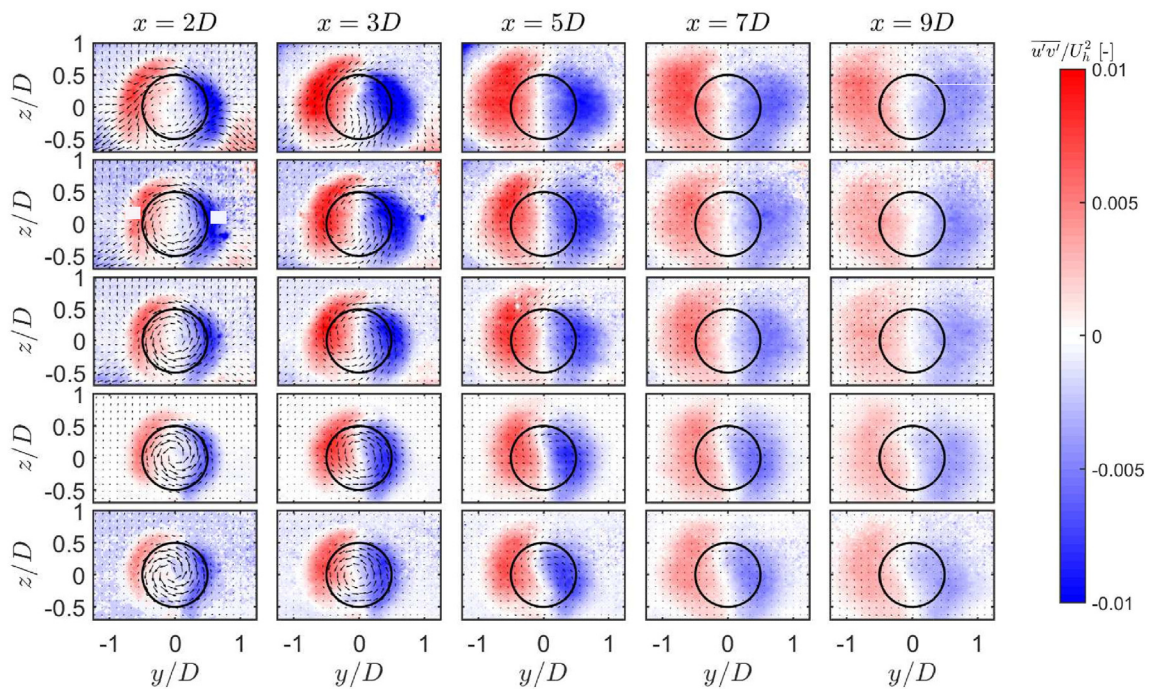


Fig. 10. Contours of the normalized lateral momentum flux in the wake of the turbine. From top to bottom: 90° Edge, 5% r/H, 10% r/H, 33° Slope, 21.5° Slope. In-plane velocity components are overlaid. Black circles represent the rotor position.

velocity induced by the escarpment in the base flow can affect the wake rotation; high vertical velocity in the base flow of the turbine sited on the 90° Edge escarpment results in a weaker rotation. As the base flow vertical velocity component reduces with the increase in the curvature of the escarpment leading edge and by the addition of the ramp, the wake rotation gets stronger in these cases. To compare the streamwise velocity deficit quantitatively, Fig. 13

shows the lateral and vertical profiles in y-z and x-z planes passing through the turbine axis. The velocity deficit is observed to be higher in the FFS cases and it also appears to recover faster than in the ramp cases.

To elaborate on the recovery of the wake center velocity deficit, we plot the maximum velocity deficit for each case as a function of the downstream distance in Fig. 14. The three FFS escarpment cases

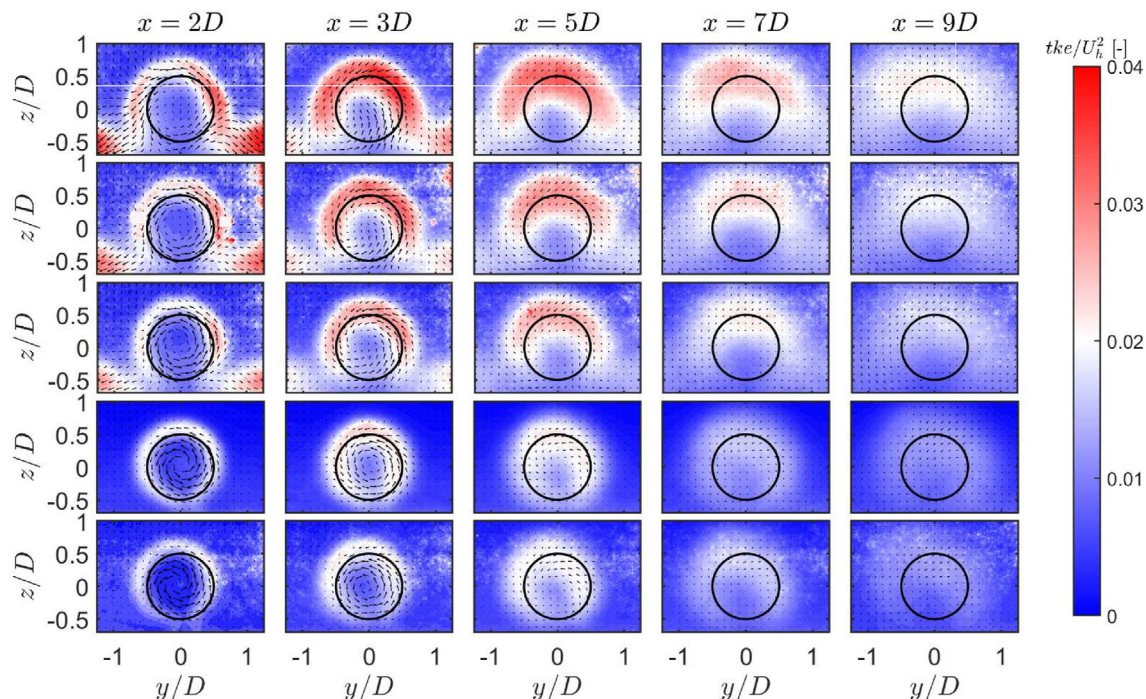


Fig. 11. Contours of the normalized turbulence kinetic energy in the wake of the turbine. From top to bottom: 90° Edge, 5% r/H, 10% r/H, 33° Slope, 21.5° Slope. In-plane velocity components are overlaid. Black circles represent the rotor position.

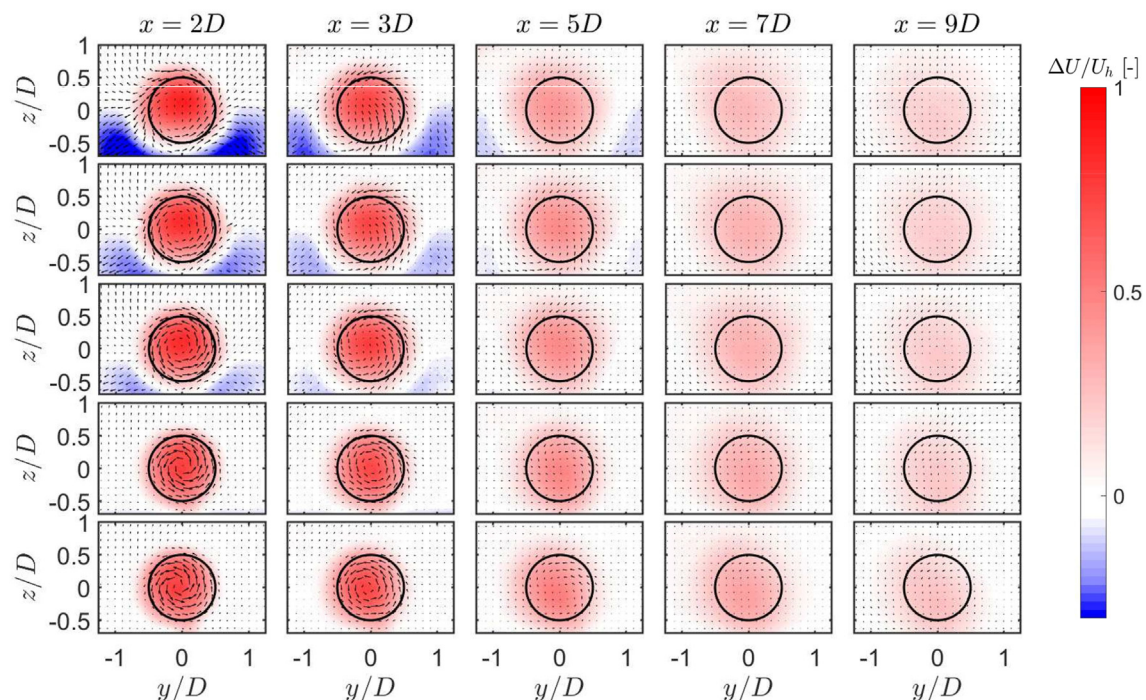


Fig. 12. Contours of the normalized averaged streamwise velocity deficit in the wake of the turbine. From top to bottom: 90° Edge, 5% r/H, 10% r/H, 33° Slope, 21.5° Slope. In-plane velocity components are overlaid. Black circles represent the rotor position.

have higher velocity deficit maxima in the near wake than the ramp-shaped escarpment cases. This can be related to the effect of pressure gradient induced by the topography on the turbine wake. As shown earlier, the thrust coefficient of the turbine is almost unchanged for different escarpments (see Fig. 7). In topography,

however, the wake velocity deficit also has a contribution from the pressure gradient induced by the terrain [76]. The streamwise variation in base flow velocity is higher in the FFS escarpments compared to the ramp-shaped ones (see Fig. 4), which implies a higher contribution from the pressure gradient, and thereby, a

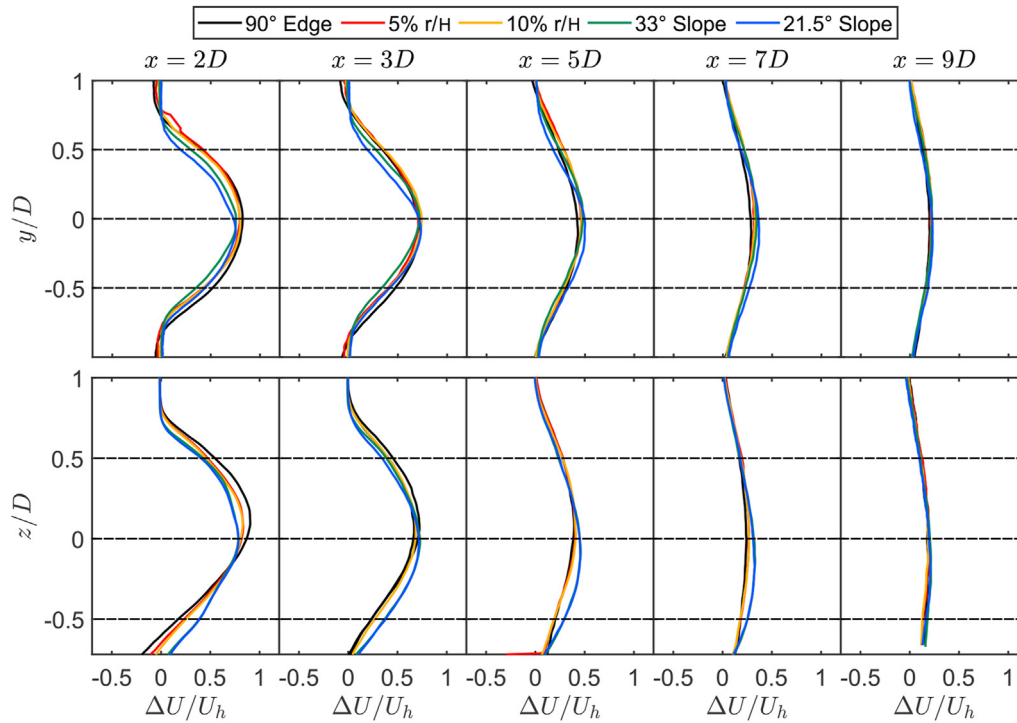


Fig. 13. Normalized averaged streamwise velocity deficit: lateral (top) and vertical (bottom) profiles passing through the turbine axis. Horizontal dashed lines trace the rotor axis and tip positions.

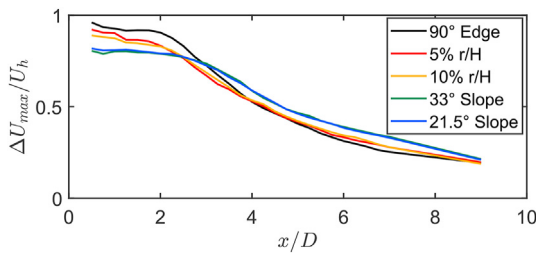


Fig. 14. Maximum velocity deficit as a function of downstream distance.

higher wake velocity deficit. The maximum velocity deficit also shows a minimal change in this near wake region. This is because the shear layer around the rotor tips, which brings outer flow into the wake, has not grown enough to re-energize the wake center. In the far wake, the recovery of the wake center velocity deficit is faster for the FFS cases compared to that for the ramp-shape cases. This is due to the higher levels of turbulence and momentum fluxes for the FFS cases compared to the ramp-shaped escarpment cases. The far wake region is also characterized by the Gaussian profile of the velocity deficit and linear expansion of the wake with the increase in the downstream distance. Both characteristics will be discussed later in this section.

To understand the impact of the wind turbine on the streamwise turbulence intensity in the wake, we compute the added streamwise turbulence intensity as follows:

$$I_{add} = \begin{cases} +\sqrt{I_{u,w}^2 - I_{u,b}^2}, & I_{u,w} \geq I_{u,b}, \\ -\sqrt{I_{u,b}^2 - I_{u,w}^2}, & I_{u,w} < I_{u,b}, \end{cases}$$

where $I_{u,b}$ and $I_{u,w}$ are the streamwise turbulence intensities

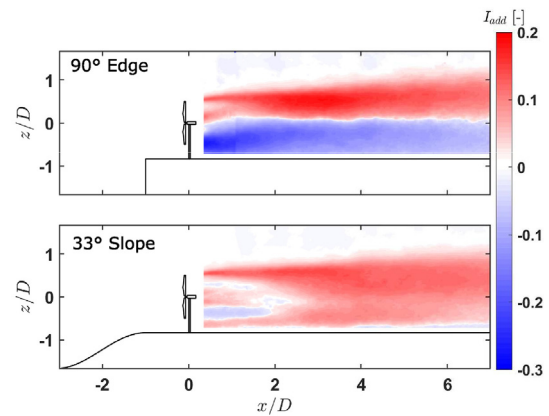


Fig. 15. Contours of the added streamwise turbulence intensity in the turbine wake for two selected cases.

without and with the turbine at the same physical location. Fig. 15 shows the streamwise contours of added streamwise turbulence intensity for two selected cases. The added turbulence intensity is positive in the upper half of the rotor due to high turbulence production behind the rotor tip. Its magnitude is larger for the FFS escarpment compared to the ramp-shaped escarpment. The magnitude of I_{add} is highest at a downstream distance of around 3D where the *tke* production is highest and the transition from near to far wake happens. The I_{add} is observed to be negative below the turbine hub height for the FFS escarpment throughout the downstream extent of the domain, whereas in the ramp-shaped escarpment it is positive except for a small region around the rotor bottom tip in the near wake region. Change in the flow shear close to the rotor bottom tip is responsible for the negative I_{add} in the ramp-shaped escarpment. In the FFS escarpment, the negative

I_{add} appears because the high turbulence intensity region generated due to the flow shear induced by the leading edge flow separation in the base flow is suppressed in the wake flow due to the change in the flow shear caused by the turbine.

For a quantitative comparison between all cases, profiles of I_{add} in lateral and vertical planes passing through the turbine axis are plotted in Fig. 16. The FFS escarpment cases show a gradual decrease in the magnitude of the added turbulence intensity with the increase in the curvature. The two ramp cases have a lower magnitude of the added turbulence intensity compared to the FFS cases and show very similar values compared to each other.

Another important characteristic of the turbine wakes is their rate of expansion as a function of the downstream distance, known as the wake growth rate. The wake is shown to grow linearly in the far wake [11,79] and, therefore, its width can be estimated by the following relation:

$$\frac{\sigma}{D} = k \frac{x}{D} + \epsilon, \tag{4}$$

where the slope k of the linear relation is the wake growth rate and ϵ is the initial wake width. The wake width σ , defined as the standard deviation of the Gaussian fit to the lateral and vertical velocity deficit profiles, is plotted in Fig. 17. A linear fit is done on the normalized standard deviation, the slope of which yields the wake growth rate k . As can be seen, the wake growth rate in the lateral direction is similar for all the cases. In the vertical direction, however, the 90° Edge case shows the highest wake growth rate, with values gradually decreasing for the rest of the cases. A relatively higher mean flow shear and enhancement of turbulence in the vertical direction, compared to that in the lateral direction, can

explain the observed trend. Fig. 18 shows the maxima of the vertical and lateral turbulence intensities in the vertical and lateral profiles at the turbine centerline and hub height, respectively. The vertical turbulence intensity is observed to be higher than the lateral one in the FFS cases, whereas their difference decreases in the ramp-shaped escarpment cases. This is consistent with the larger magnitude of the momentum fluxes and, consequently, the wake growth rates in the vertical direction compared with the lateral one. This is, however, in contrast with what is reported over flat terrain, where the momentum fluxes and, thus, the wake growth rates are higher in the lateral direction compared to the vertical one [10,78].

Finally, wind turbine wakes are known to depict self-similar behavior in both flat [10,29,30] and complex [59] terrains. Here, we plot the normalized streamwise velocity deficit profiles as a function of distance from the wake center normalized by the wake half-width $r_{1/2}$. The wake half-width is defined as the distance from the velocity deficit maximum to the point where the velocity deficit is reduced to 50% of its maximum value. We verify that the self-similarity holds for both vertical and lateral profiles in all escarpment cases and the velocity deficit can be approximated by a Gaussian profile (see Fig. 19). This is important, especially for the FFS escarpments, as it shows that the interaction between the wake and flow separation does not affect the self-similarity of the velocity deficit in the far wake.

3.5. Comparison of experimental and analytically modeled velocity deficit profiles

In this section, we test an existing analytical tool to model wakes

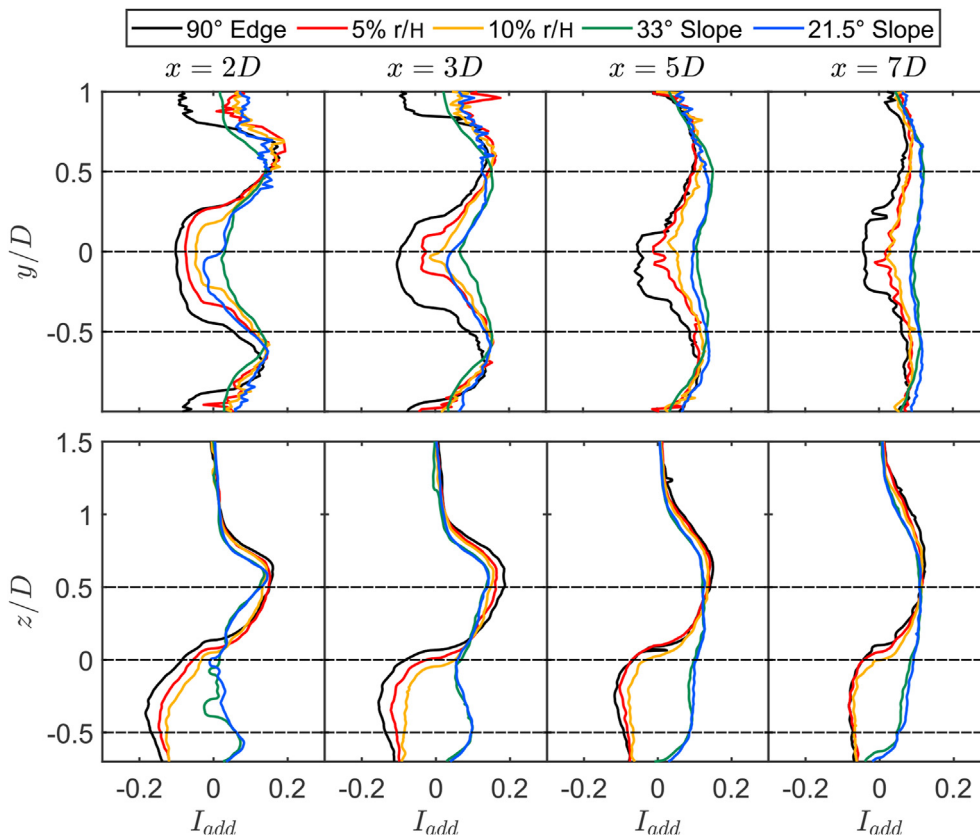


Fig. 16. Added streamwise turbulence intensity: lateral (top) and vertical (bottom) profiles passing through the turbine axis. Horizontal dashed lines trace rotor axis and tip positions.

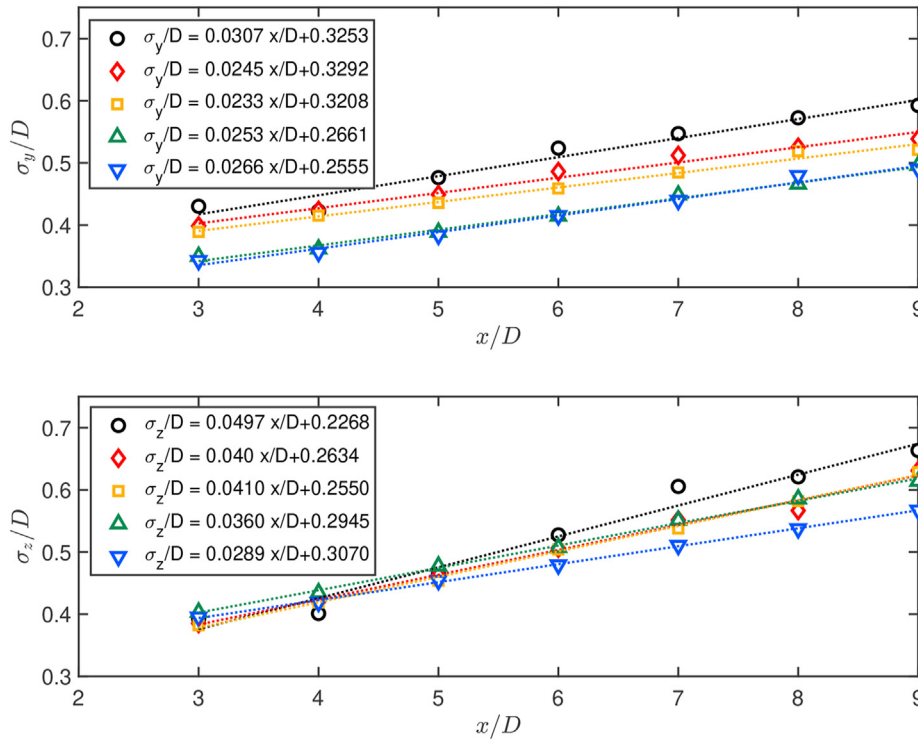


Fig. 17. Normalized standard deviation of the streamwise velocity deficit for the lateral (top) and vertical (bottom) profiles at the turbine hub height and centerline, respectively. Black: 90° Edge; orange: 5% r/H ; red: 10% r/H ; green: 33° Slope; blue: 21.5° Slope. The legend shows the linear fits according to equation (4) for each case.

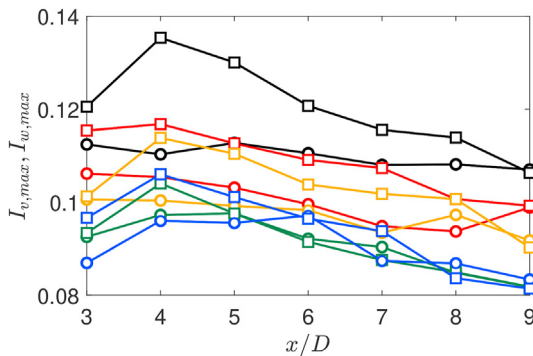


Fig. 18. Maximum of the lateral and vertical turbulence intensity in the lateral and vertical direction at the turbine hub height and centerline, respectively. The circles and squares represent the lateral and vertical turbulence intensity values, respectively.

behind wind turbines sited on escarpments. The problem under focus is stated as: given that the mean streamwise velocity at the hub height in the base flow $U_b(x)$ is known, can we then predict the wake using an analytical model? The dominating effect of the escarpment on the flow is a pressure gradient that is induced due to the presence of the topography. Therefore, we choose the model for turbulent axisymmetric wakes under a pressure gradient proposed by Shamsoddin & Porté-Agel [76]. For details on the model, the reader is referred to the original work; here, we will briefly describe the procedure followed to obtain the velocity deficit profiles.

We generate a velocity profile using the power law fit in Fig. 3 to represent the upstream flow. For model inputs, we choose a thrust coefficient C_T of 0.8 (Fig. 7). The wake width $\sigma_0(x)$ for the miniature wind turbine is computed using the linear relation in equation (4), where the wake growth rate is estimated using the empirical relation $k = 0.3TI$ [80] and TI is the rotor averaged turbulence

intensity in the base flow at the turbine location; and ε is taken equal to $1/\sqrt{8}$ [81]. Using these parameters, the model returns the maximum velocity deficit under zero pressure gradient C_0 :

$$C_0(x) = 1 - \sqrt{1 - \frac{C_T}{8 \left(\frac{\sigma_0(x)}{D}\right)^2}}, \quad (5)$$

and the invariant ratio of velocity deficit to wake width:

$$\Lambda_0(x) = \Lambda(x) = \frac{C_0(x)U_{in}}{\sigma_0(x)}, \quad (6)$$

where U_{in} is the upstream velocity at the hub height, Λ_0 is the invariant ratio under zero pressure gradient and Λ is the invariant ratio under pressure gradient. As a next step, the base flow information and the invariant ratio are used to compute the maximum velocity deficit C under the pressure gradient induced by the escarpments:

$$\frac{dC(x)}{dx} = \frac{-1}{\left(\frac{U_b}{\Lambda_0}\right)(3C^2 - 2C^3)} \left[\frac{1}{4} \frac{dU_b^4}{dx} \frac{C^3}{\Lambda_0^2} + (C^3 - \frac{C^4}{2}) \frac{d}{dx} \left(\frac{U_b^4}{\Lambda_0^2}\right) \right], \quad (7)$$

with the following boundary condition:

$$C(x_i) = C_0(x_i), \quad (8)$$

where x_i represents the start of the far wake, taken as the streamwise position where the maximum velocity deficit (in experiments) is equal to the theoretical value $(1 - \sqrt{1 - C_T})$. Furthermore, the wake width $\sigma(x)$ is computed using the new velocity deficit and base flow information:

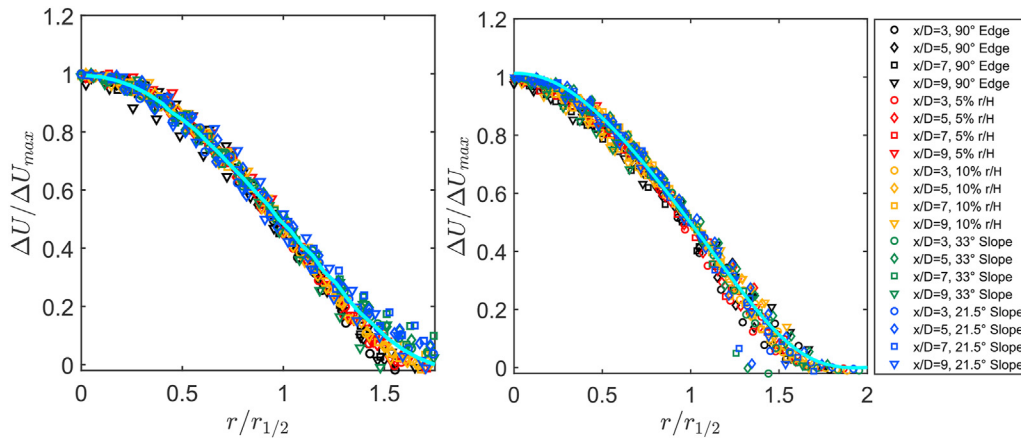


Fig. 19. Self-similar normalized streamwise velocity deficit lateral (left) and vertical (right) profiles at the turbine hub height and centerline, respectively. A Gaussian curve is overlaid for comparison.

$$\sigma(x) = \frac{U_b(x)C(x)}{\Lambda(x)} \tag{9}$$

Finally, the velocity deficit profiles are computed using the Gaussian shape function:

$$\frac{U_b(x) - U_w(x, r)}{U_b(x)} = C(x)e^{-\left(\frac{r^2}{2\sigma^2}\right)}, \tag{10}$$

where U_w is the streamwise velocity in the wake and r is the radial distance from the maximum velocity deficit position. It is to be noted that the turbine wakes in the current study are not perfectly axisymmetric and experience flow shear in the vertical direction due to the effect of the surface. As stated by Shamsoddin & Porté-Agel [76], in such case the wake width obtained from the model is the equivalent wake width of the lateral and vertical wake widths, which is computed as the geometric mean of the two wake widths: $\sigma_{eq} = \sqrt{\sigma_y \sigma_z}$.

Fig. 20 shows the comparison between the experimentally and analytically obtained maximum velocity deficit and equivalent wake width. The degree of agreement between the experiments and the model is observed to be dependent on the escarpment shape. For the ramp-shaped escarpment cases, the maximum velocity deficit is predicted reasonably well, with slight underestimation until a downstream distance of 4.75 rotor diameters. For the forward facing step cases, however, the velocity deficit prediction gets worse with the increase in the edge sharpness. The escarpment with 10% curvature at the edge (with respect to the escarpment height) shows good agreement between the experiments and the

model beyond 5 rotor diameters. The other two forward facing step escarpments show an underestimation of the maximum velocity deficit by the model, with the highest difference for a case with a sharp edge. The equivalent wake width shows a similar trend, with the best agreement between the experiments and the model in ramp-shaped escarpment cases and worst in the sharp-edged escarpment. The equivalent wake width is observed to be underestimated by the model.

Finally, a comparison of the averaged streamwise velocity deficit profiles is shown in Fig. 21. As can be seen, the velocity deficit are well reproduced for the ramp-shaped escarpments and forward facing step with 10% curvature beyond 5 rotor diameters, even though the effect of wake width underestimation is seen in the vertical profiles. For the rest of the two forward facing step cases, an underestimation of velocity deficit profiles is observed.

The underestimation of the maximum velocity deficit, as well as the equivalent wake width in some cases (as shown in Fig. 20) can be related to the fact that the analytical model used here assumes no pressure gradient in the base flow at the turbine location. This assumption is embedded in the boundary condition given in equation (8). In the ramp-shaped escarpments, the pressure gradient imposed by the base flow at the turbine location is not very high, which is why the model gives acceptable results. In the forward facing step escarpments, the agreement between the model and experiments gets worse with the increase in the sharpness of the escarpment edge. As a sharper edge induces a higher pressure gradient via the base flow at the turbine location, the difference between the model and the experiments gets higher. This highlights the need to develop analytical models capable of capturing pressure gradient effects in the base flow at the turbine

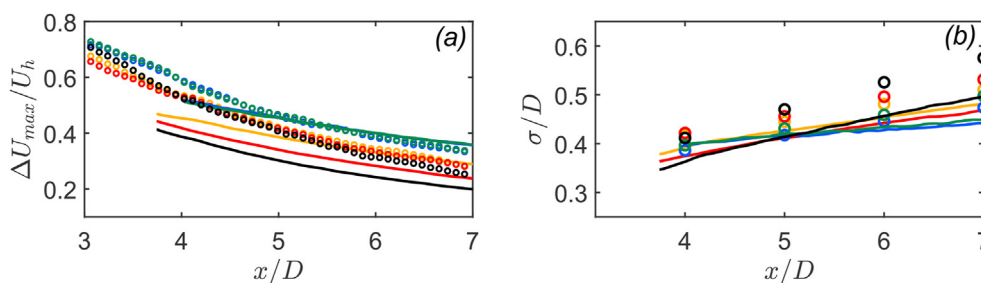


Fig. 20. Comparison of the maximum normalized streamwise velocity deficit (a) and the equivalent wake width (b) between the analytical model and experiments. Circles mark the experimental data and solid lines represent the PG model. Color codes for different cases are same as Fig. 17.

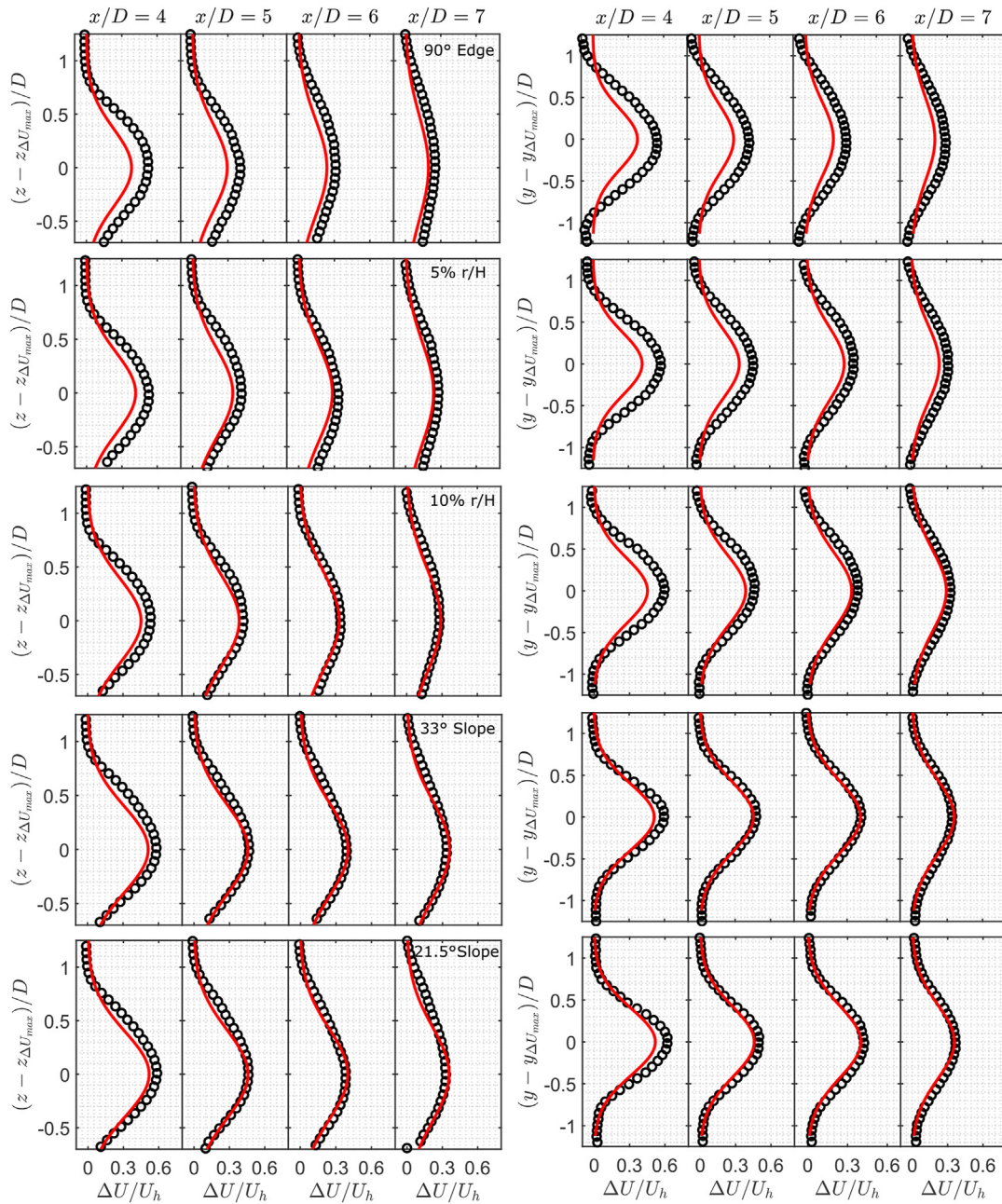


Fig. 21. Comparison of the normalized averaged streamwise velocity deficit profiles between the analytical models and experiments for different cases. Experimental data is marked by circles and solid line represents the PG model.

location.

3.6. Wake meandering and trajectory

Defined by low-frequency and large-scale coherent oscillations, meandering is an important dynamical feature of the wake, contributing to the unsteady wake dynamics. To characterize meandering of the turbine wake over different escarpments, we employ a ‘center of mass’ method [78,82,83]. The method quantifies the displacement of the center of the instantaneous velocity deficit in the lateral and vertical directions using the following equations:

$$y_c = \frac{\iint \Delta U y dy dz}{\iint \Delta U dy dz}, \tag{11}$$

$$z_c = \frac{\iint \Delta U z dy dz}{\iint \Delta U dy dz}. \tag{12}$$

The information on the instantaneous wake center location in the lateral and vertical direction is then used to compute the joint probability density function (PDF) for different cases. Fig. 22 shows the joint PDFs for two cases at different streamwise locations. In general, the spread of the instantaneous wake centers is observed to increase with the downstream distance. This spread is higher in

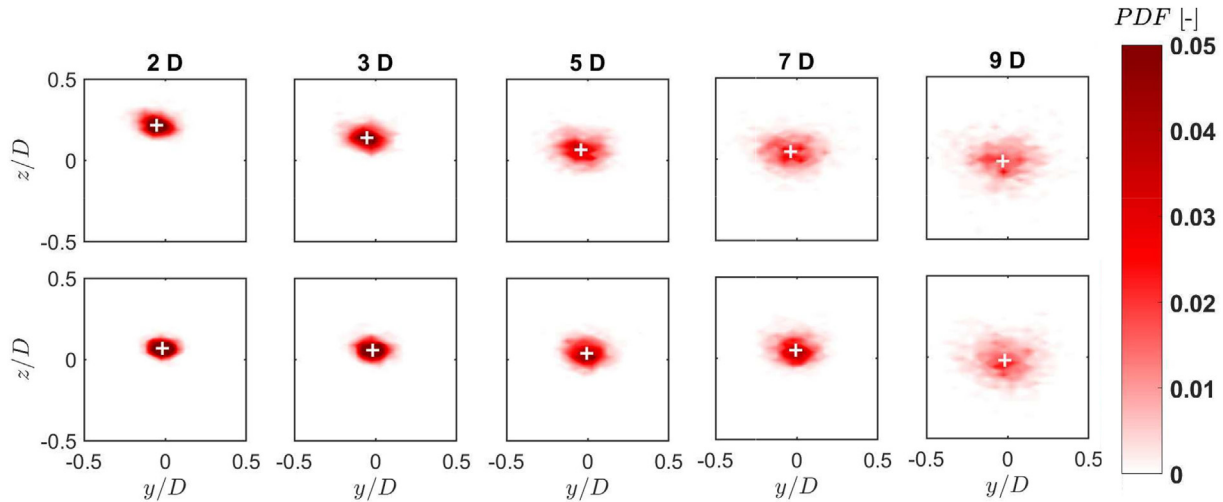


Fig. 22. Normalized joint probability density function of the instantaneous wake center at different downstream locations for the 90° Edge (top row) and 33° Slope (bottom row). Plus signs indicate the mean wake center.

the lateral direction compared to the vertical one. The spread in the joint PDFs is higher for the turbine on the FFS escarpment compared to that for the turbine on the ramp-shaped escarpment. This indicates that the FFS escarpment enhances the meandering of the wake compared to the ramp-shape escarpment. The unsteady nature of the flow separation in the base flow of the FFS escarpment can explain the relatively higher meandering observed in this case.

Another important observation is the vertical displacement of the mean wake center from the turbine axis in Fig. 22. In the near wake, the mean wake center is shifted above the turbine axis, followed by a gradual downward shift with the increase in the downstream distance. This mean wake center displacement is comparatively higher for the turbine on the FFS escarpment than for the one on the ramp-shaped escarpment. In addition, the wake trajectory, defined as the vertical position of the maximum velocity deficit $z_{\Delta U_{max}}$ at each streamwise location, is plotted in Fig. 23 for all the cases. The wake is observed to have an upward trajectory in the near wake region with a downward shift in the far wake for the FFS escarpments. For the ramp-shaped escarpments, however, the wake is more attached to the surface and shows a lower trajectory than for the three FFS escarpments. In order to understand this, we first look at the normalized vertical velocity component without the turbine in Fig. 24 (a). The vertical velocity component in the base flow is much higher for the turbine on the FFS escarpment compared to the one on the ramp-shaped escarpment. This high positive vertical velocity component causes the wake to shift upward in the near-wake region for the turbine on the FFS escarpment. As the difference in the mean wake center between the two cases is highest at a downstream distance of 2D, we show the vertical velocity component at this position in Fig. 24 (b). In the case of the ramp-shaped escarpment, the vertical velocity component is

solely caused by the wake rotation, with positive and negative vertical velocity in the right and left halves of the wake, respectively. In the case of the FFS escarpment, however, there is a positive vertical velocity component around the center of the rotor. This positive vertical velocity component is a result of the higher vertical velocity faced by the turbine, and pushes the wake center in the upward direction for the turbine on the FFS escarpment.

3.7. Counter-rotating vortex pair and energy entrainment

The non-zero mean vertical velocity component in the base flow also leads to the development of a counter-rotating vortex pair (CVP) in the far wake of the wind turbines sited on the escarpments. The CVP is fully developed in the case of the sharp edge escarpment; therefore, we will focus on the mentioned case in this section. To visualize the formation of the CVP, we show the normalized out-of-plane vorticity in Fig. 25. In the near wake, there is an outward flow from the wake, which creates a negative vorticity region surrounding the rotor. However, as we move downstream ($x/D = 3$), the positive vertical velocity component around the top of the wake diminishes and we observe outer flow moving into the wake due to the presence of a negative vorticity region at the top of the wake. In the far wake, the distribution of the in-plane velocity components becomes almost perpendicular to the surface at the turbine center, depicting a strong vertical component. This vertical velocity component is positive in the region under the rotor center and negative above it, and is believed to give rise to the development of the CVP in order to satisfy continuity. This mechanism is similar to the one observed by Bastankhah & Porté-Agel [81] in yawed wind turbines, where the formation of a CVP is due to the strong lateral velocity component.

It is to be noted that the vertical velocity component is not as high as the lateral velocity component in yawed turbines, such that it does not cause a significant distortion in the shape of the wake. However, it does appear to play a role in the entrainment of energy from the outer flow into the wake and, thus, contributes to the re-energization of the wake. To explain this, we show two dimensional fields of the advection term of mean kinetic energy in Fig. 26. The advection term is negative in the near wake surrounding the rotor area, where the vorticity is negative, showing an outward flow of energy. As we move downstream, however, when the formation of the vortex pair starts bringing outer flow into the wake, the

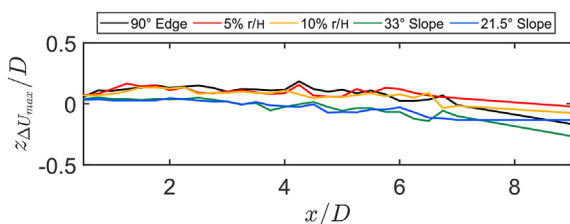


Fig. 23. Wake trajectory as a function of the downstream distance.

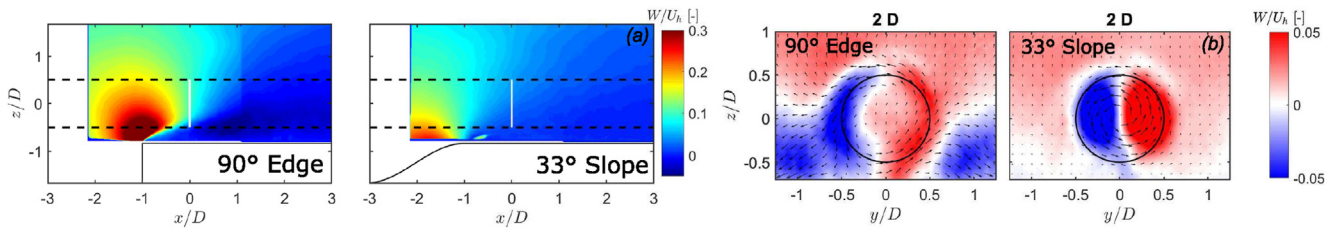


Fig. 24. (a) Contours of the normalized averaged vertical velocity component on the escarpments without the turbine. White vertical line shows the position of the prospective turbine. (b) Contours of the normalized averaged vertical velocity component at a distance of 2D in the wake of the turbine. The black circle indicates the rotor outline.

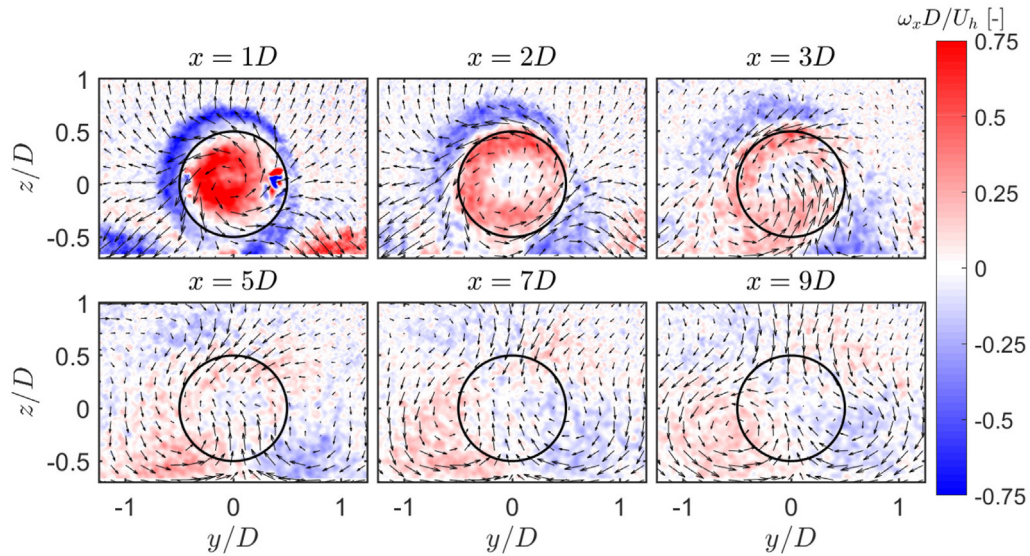


Fig. 25. Contours of the normalized out-of-plane vorticity with in-plane velocity vectors overlaid for the 90° Edge escarpment. The black circle indicates the rotor outline.

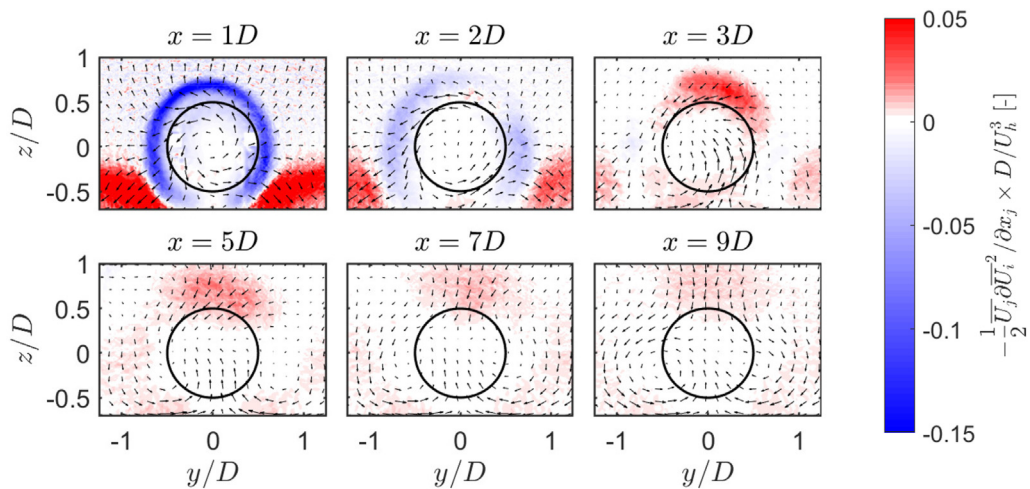


Fig. 26. Contours of the normalized advection of mean kinetic energy with in-plane velocity vectors overlaid for the 90° Edge escarpment. The black circle indicates the rotor outline.

advection term becomes positive at the rotor top and around the vortex cores, leading to a faster wake recovery in the far wake.

4. Summary

Onshore wind energy has grown tremendously over the last two decades, with wind farms often located in complex terrain. Lack of

adequate knowledge of wind turbine behavior in such challenging terrains is known to result in inaccurate estimation of power performance and dynamic loads. Understanding wakes in complex terrain, therefore, has become crucial in today's renewable energy market for better resource assessment, power optimization and layout design of wind farms in such sites. In the current study, we have characterized the wake generated by a single wind turbine

sited on different escarpments using stereo-PIV measurements. Escarpments are a common topographical feature and a potential location for wind farms.

Focusing on the sensitivity of the wind turbine wake to the geometrical details of the topography, we have studied five different escarpment models approximated by forward facing steps (FFS) and ramp-shaped escarpments. The shape of the escarpment leading edge is found to have a strong influence on the base flow (flow without the turbine) velocity, shear, speed-up and turbulence over the topography, which eventually have an impact on the wake of the turbine. The presence of the turbine suppresses the development of the flow recirculation near the surface in the wake for the FFS escarpments, and the normalized streamwise velocity in the turbine wake is lowest for the FFS with a sharp edge.

The turbine wake velocity deficit shows fastest recovery and the turbulence kinetic energy is observed to be highest in the case of the FFS with a sharp edge, which is consistent with the highest magnitude of momentum fluxes in this case. By adding a curvature as little as 5% at the leading edge with respect to the escarpment height, the turbulence kinetic energy is significantly reduced compared to the sharp edge case. The turbine wake on the ramp-shaped escarpments shows lower turbulence kinetic energy than the one on the FFS escarpments. Consistent with the amount of turbulence in the base flow, the near wake length is also observed to be shorter for the turbine on the FFS escarpments compared to that on the ramp-shaped escarpments. The streamwise added turbulence intensity in the wake shows that, in comparison to the base flow, the turbine suppresses the production of turbulence below the hub height and enhances it above the hub height for the FFS escarpments. This is because the shear layer formed due to the leading edge flow separation is suppressed in the turbine wake. For the ramp-shaped escarpments, however, the wake flow is more turbulent compared to the base flow except for a small region around the rotor bottom tip level in the near wake region. The wake growth rate in the lateral direction is found to be very similar in all cases; in contrast, it differs in the vertical direction. The vertical growth rate is also observed to be higher than the lateral one, which is related to a comparatively higher turbulence and mean flow shear in the vertical direction compared to the lateral one in the turbine wake. The velocity deficit profiles show self-similarity in the far wake for all the cases.

We have also assessed an analytical model for the prediction of velocity deficit in the wake of the turbine sited on escarpments. It is found that, the performance of the model depends on the escarpment shape, as the model works reasonably well for the ramp-shaped escarpments, but underestimates the maximum velocity deficit and wake width for the forward facing step cases. This is due to the fact that the analytical model assumes no pressure gradient induced by the base flow at the turbine location, whereas in the forward facing step cases the induced pressure gradient by the base flow at the turbine location is not negligible. Future research should address this limitation of the analytical model.

The shape of the escarpment is also observed to affect the instantaneous location of the turbine wake center and, thereby, the dynamics of wake meandering, with higher meandering in the FFS escarpments compared to the ramp-shaped ones. This is associated with the unsteadiness of the base flow, which is higher for the FFS due to the dynamic nature of the flow separation. The center of the wake is shifted above the turbine hub height in the near wake of the turbine on the FFS escarpment, with a gradual downward shift in the far wake. This is associated with a higher vertical velocity component in the base flow. The relatively large vertical velocity component also leads to the formation of a counter-rotating vortex pair in the far wake of the 90° Edge FFS escarpment, which plays a role in the energy entrainment from the outer flow into the wake.

Funding

This research was funded by the Swiss National Science Foundation (grant number: 200021_172538) and the Swiss Federal Office of Energy (grant number: SI/502135-01). In addition, this project was carried out within the frame of the Swiss Centre for Competence in Energy Research on the Future Swiss Electrical Infrastructure (SCCER-FURIES) with the financial support of the Swiss Innovation Agency (Innosuisse - SCCER programme, contract number: 1155002544).

CRedit authorship contribution statement

Arslan Salim Dar: Conceptualization, Methodology, Investigation, Data curation, Formal analysis, Writing – original draft, Visualization. **Fernando Porté-Agel:** Conceptualization, Methodology, Supervision, Resources, Writing – review & editing, Funding acquisition.

Declaration of competing interest

The authors declare that they have no known competing financial interests or personal relationships that could have appeared to influence the work reported in this paper.

References

- [1] GWEC. Global Wind Report 2019, Global wind energy council, 2020.
- [2] IRENA. Renewable Power Generation Costs in 2019, International Renewable Energy Agency, Abu Dhabi, 2020.
- [3] F. Porté-Agel, M. Bastankhah, S. Shamsoddin, Wind-turbine and wind-farm flows: a review, *Boundary-Layer Meteorol.* 174 (2020) 1–59.
- [4] R.J. Stevens, C. Meneveau, Flow structure and turbulence in wind farms, *Annu. Rev. Fluid Mech.* 49 (2017) 311–339.
- [5] N. Troldborg, J.N. Sørensen, R. Mikkelsen, Numerical simulations of wake characteristics of a wind turbine in uniform inflow, *Wind Energy: Int. J. Progr. Appl. Wind Power Conv. Technol.* 13 (1) (2010) 86–99.
- [6] D. Medici, P.H. Alfredsson, Measurements on a wind turbine wake: 3D effects and bluff body vortex shedding, *Wind Energy: Int. J. Progr. Appl. Wind Power Conv. Technol.* 9 (3) (2006) 219–236.
- [7] L.P. Chamorro, F. Porté-Agel, A wind-tunnel investigation of wind-turbine wakes: boundary-layer turbulence effects, *Boundary-Layer Meteorol.* 132 (2009) 129–149.
- [8] H. Hu, Z. Yang, P. Sarkar, Dynamic wind loads and wake characteristics of a wind turbine model in an atmospheric boundary layer wind, *Exp. Fluids* 52 (2012) 1277–1294.
- [9] M. Bastankhah, F. Porté-Agel, Wind tunnel study of the wind turbine interaction with a boundary-layer flow: upwind region, turbine performance, and wake region, *Phys. Fluids* 29 (6) (2017), 065105.
- [10] M. Abkar, F. Porté-Agel, Influence of atmospheric stability on wind-turbine wakes: a large-eddy simulation study, *Phys. Fluids* 27 (3) (2015), 035104.
- [11] L.P. Chamorro, F. Porté-Agel, Effects of thermal stability and incoming boundary-layer flow characteristics on wind-turbine wakes: a wind-tunnel study, *Boundary-Layer Meteorol.* 136 (3) (2010) 515–533.
- [12] K. Bhaganagar, M. Debnath, Implications of stably stratified atmospheric boundary layer turbulence on the near-wake structure of wind turbines, *Energies* 7 (9) (2014) 5740–5763.
- [13] L. Vollmer, G. Steinfeld, D. Heinemann, M. Kühn, Estimating the wake deflection downstream of a wind turbine in different atmospheric stabilities: an LES study, *Wind Energy Sci.* 1 (2016) 129–141.
- [14] M. Abkar, F. Porté-Agel, Influence of the Coriolis force on the structure and evolution of wind turbine wakes, *Phys. Rev. Fluids* 1 (6) (2016), 063701.
- [15] M. Calaf, C. Meneveau, J. Meyers, Large eddy simulation study of fully developed wind-turbine array boundary layers, *Phys. Fluids* 22 (1) (2010), 015110.
- [16] F. Porté-Agel, Y.T. Wu, H. Lu, R.J. Conzemius, Large-eddy simulation of atmospheric boundary layer flow through wind turbines and wind farms, *J. Wind Eng. Ind. Aerod.* 99 (4) (2011) 154–168.
- [17] M. Abkar, A. Sharifi, F. Porté-Agel, Wake flow in a wind farm during a diurnal cycle, *J. Turbul.* 17 (4) (2016) 420–441.
- [18] D. Allaerts, J. Meyers, Large eddy simulation of a large wind-turbine array in a conventionally neutral atmospheric boundary layer, *Phys. Fluids* 27 (6) (2015), 065108.
- [19] M. Abkar, F. Porté-Agel, Mean and turbulent kinetic energy budgets inside and above very large wind farms under conventionally-neutral condition, *Renew. Energy* 70 (2014) 142–152.

- [20] E.H. Camp, R.B. Cal, Mean kinetic energy transport and event classification in a model wind turbine array versus an array of porous disks: energy budget and octant analysis, *Phys. Rev. Fluids* 1 (4) (2016), 044404.
- [21] M.P. van der Laan, N.N. Sørensen, Why the Coriolis force turns a wind farm wake clockwise in the Northern Hemisphere, *Wind Energy Sci.* 2 (1) (2017) 285–294.
- [22] L.P. Chamorro, R.E.A. Arndt, F. Sotiropoulos, Turbulent flow properties around a staggered wind farm, *Boundary-Layer Meteorol.* 141 (3) (2011) 349–367.
- [23] F. Porté-Agel, Y.T. Wu, C.H. Chen, A numerical study of the effects of wind direction on turbine wakes and power losses in a large wind farm, *Energies* 6 (10) (2013) 5297–5313.
- [24] S. Baidya Roy, S.W. Pacala, R.L. Walko, Can large wind farms affect local meteorology? *J. Geophys. Res.: Atmospheres* 109 (D19) (2004).
- [25] S.B. Roy, Simulating impacts of wind farms on local hydrometeorology, *J. Wind Eng. Ind. Aerod.* 99 (4) (2011) 491–498.
- [26] M. Calaf, C. Higgins, M.B. Parlange, Large wind farms and the scalar flux over an heterogeneously rough land surface, *Boundary-Layer Meteorol.* 153 (3) (2014) 471–495.
- [27] S.K. Siedersleben, J.K. Lundquist, A. Platis, J. Bange, K. Bärfuss, A. Lampert, B. Cañadillas, T. Neumann, S. Emeis, Micrometeorological impacts of offshore wind farms as seen in observations and simulations, *Environ. Res. Lett.* 13 (12) (2018) 124012.
- [28] I. Katic, J. Højstrup, N.O. Jensen, A Simple Model for Cluster Efficiency, *European Wind Energy Association Conference and Exhibition*, 1986, p. 407410. October.
- [29] S. Xie, C. Archer, Self-similarity and turbulence characteristics of wind turbine wakes via large-eddy simulation, *Wind Energy* 17 (2014) 657669.
- [30] M. Bastankhah, F. Porté-Agel, A new analytical model for wind-turbine wakes, *Renew. Energy* 70 (2014) 116–123.
- [31] M. Abkar, J.N. Sørensen, F. Porté-Agel, An analytical model for the effect of vertical wind veer on wind turbine wakes, *Energies* 11 (2018) 1838.
- [32] A. Niayifar, F. Porté-Agel, Analytical modeling of wind farms: a new approach for power prediction, *Energies* 9 (9) (2016) 741.
- [33] R.J. Stevens, D.F. Gayme, C. Meneveau, Coupled wake boundary layer model of wind-farms, *J. Renew. Sustain. Energy* 7 (2) (2015), 023115.
- [34] R.J. Stevens, D.F. Gayme, C. Meneveau, Generalized coupled wake boundary layer model: applications and comparisons with field and LES data for two wind farms, *Wind Energy* 19 (11) (2016) 2023–2040.
- [35] P.S. Jackson, J.C.R. Hunt, Turbulent wind flow over a low hill, *Q. J. R. Meteorol. Soc.* 101 (430) (1975) 929–955.
- [36] P.J. Mason, R.I. Sykes, Flow over an isolated hill of moderate slope, *Q. J. R. Meteorol. Soc.* 105 (444) (1979) 383–395.
- [37] J.R. Pearse, D. Lindley, D.C. Stevenson, Wind flow over ridges in simulated atmospheric boundary layers, *Boundary-Layer Meteorol.* 21 (1) (1981) 77–92.
- [38] T. Ishihara, K. Hibii, S. Oikawa, A wind tunnel study of turbulent flow over a three-dimensional steep hill, *J. Wind Eng. Ind. Aerod.* 83 (1–3) (1999) 95–107.
- [39] T. Takahashi, S. Kato, S. Murakami, R. Ooka, M.F. Yassin, R. Kono, Wind tunnel tests of effects of atmospheric stability on turbulent flow over a three-dimensional hill, *J. Wind Eng. Ind. Aerod.* 93 (2) (2005) 155–169.
- [40] T.L. Clark, A small-scale dynamic model using a terrain-following coordinate transformation, *J. Comput. Phys.* 24 (2) (1977) 186–215.
- [41] F. Wan, F. Porté-Agel, Large-eddy simulation of stably-stratified flow over a steep hill, *Boundary-Layer Meteorol.* 138 (3) (2011) 367–384.
- [42] P.A. Taylor, H.W. Teunissen, The Askervein Hill project: overview and background data, *Boundary-Layer Meteorol.* 39 (1–2) (1987) 15–39.
- [43] R.E. Mickle, N.J. Cook, A.M. Hoff, N.O. Jensen, J.R. Salmon, P.A. Taylor, H.W. Teunissen, The Askervein hill project: vertical profiles of wind and turbulence, *Boundary-Layer Meteorol.* 43 (1–2) (1988) 143–169.
- [44] J. Berg, J. Mann, A. Bechmann, M.S. Courtney, H.E. Jørgensen, The Bolund experiment, part I: flow over a steep, three-dimensional hill, *Boundary-Layer Meteorol.* 141 (2) (2011) 219.
- [45] A. Bechmann, N.N. Sørensen, J. Berg, J. Mann, P.E. Réthoré, The Bolund experiment, part II: blind comparison of microscale flow models, *Boundary-Layer Meteorol.* 141 (2) (2011) 245.
- [46] A.J. Bowen, D. Lindley, A wind-tunnel investigation of the wind speed and turbulence characteristics close to the ground over various escarpment shapes, *Boundary-Layer Meteorol.* 12 (3) (1977) 259–271.
- [47] J. Lange, J. Mann, J. Berg, D. Parvu, R. Kilpatrick, A. Costache, H. Hangan, For wind turbines in complex terrain, the devil is in the detail, *Environ. Res. Lett.* 12 (9) (2017), 094020.
- [48] J. Rowcroft, D. Burton, H. Blackburn, J. Sheridan, Siting wind turbines near cliffs: the effect of ruggedness, *J. Fluid Eng.* 141 (3) (2019).
- [49] E.S. Politis, J. Prospathopoulos, D. Cabezón, K.S. Hansen, P.K. Chaviaropoulos, R.J. Barthelme, Modeling wake effects in large wind farms in complex terrain: the problem, the methods and the issues, *Wind Energy* 15 (1) (2012) 161–182.
- [50] W. Tian, A. Ozbay, W. Yuan, P. Sarakar, H. Hu, W. Yuan, An Experimental Study on the Performances of Wind Turbines over Complex Terrain. *AIAA Paper*, (2013-0612), 2013.
- [51] S. Shamsoddin, F. Porté-Agel, Large-eddy simulation of atmospheric boundary-layer flow through a wind farm sited on topography, *Boundary-Layer Meteorol.* 163 (1) (2017) 1–17.
- [52] A. Hyvärinen, A. Segalini, Effects from complex terrain on wind-turbine performance, *J. Energy Resour. Technol.* 139 (5) (2017), 051205.
- [53] A. Hyvärinen, A. Segalini, Qualitative analysis of wind-turbine wakes over hilly terrain, *J. Phys. Conf.* 854 (No. 1) (2017), 012023 (IOP Publishing).
- [54] J. Mann, N. Angelou, J. Arnqvist, D. Callies, E. Cantero, R.C. Arroyo, S. Ivanell, Complex terrain experiments in the new European wind atlas, *Phil. Trans. Math. Phys. Eng. Sci.* 375 (2017) 20160101, 2091.
- [55] H.J.S. Fernando, J. Mann, J.M.L.M. Palma, J.K. Lundquist, R.J. Barthelme, M. Belo-Pereira, P.M. Klein, The Perdigão: peering into microscale details of hilly terrain, *Bull. Am. Meteorol. Soc.* 100 (5) (2019) 799–819.
- [56] R. Menke, N. Vasiljevic, K.S. Hansen, A.N. Hahmann, J. Mann, Does the wind turbine wake follow the topography? A multi-lidar study in complex terrain, *Wind Energy Sci.* 3 (2) (2018) 681–691.
- [57] X. Han, D. Liu, C. Xu, W.Z. Shen, Atmospheric stability and topography effects on wind turbine performance and wake properties in complex terrain, *Renew. Energy* 126 (2018) 640–651.
- [58] R.J. Barthelme, S.C. Pryor, Automated wind turbine wake characterization in complex terrain, *Atmos. Meas. Tech.* 12 (6) (2019) 3463–3484.
- [59] A.S. Dar, J. Berg, N. Troldborg, E.G. Patton, On the self-similarity of wind turbine wakes in a complex terrain using large eddy simulation, *Wind Energy Sci.* 4 (4) (2019) 633–644.
- [60] J. Berg, N. Troldborg, N.N. Sørensen, E.G. Patton, P.P. Sullivan, Large-eddy simulation of turbine wake in complex terrain, *J. Phys. Conf.* 854 (No. 1) (2017, May), 012003 (IOP Publishing).
- [61] D. Astolfi, F. Castellani, L. Terzi, A study of wind turbine wakes in complex terrain through RANS simulation and SCADA data, *J. Sol. Energy Eng.* 140 (3) (2018), 031001.
- [62] M. Tabib, A. Rasheed, F. Fuchs, Analyzing complex wake-terrain interactions and its implications on wind-farm performance, *J. Phys. Conf.* 753 (No. 3) (2016, September), 032063 (IOP Publishing).
- [63] A. Crespo, F. Manuel, J.C. Grau, J. Hernández, A.D. Garrad, W. Palz, S. Scheller, Modelization of wind farms in complex terrain. Application to the Monteahuda wind farm, in: *Proceedings of European Community Wind Energy Conference*, Travemünde, 1993, pp. 440–443.
- [64] S. Shamsoddin, F. Porté-Agel, Wind turbine wakes over hills, *J. Fluid Mech.* 855 (2018) 671–702.
- [65] R.J. Barthelme, H. Wang, P. Doubrawa, G. Giroux, S.C. Pryor, Effects of an escarpment on flow parameters of relevance to wind turbines, *Wind Energy* 19 (12) (2016) 2271–2286.
- [66] T. Lutz, C. Schulz, P. Letzgus, A. Rettenmeier, Impact of complex orography on wake development: simulation results for the planned windforS test site, *J. Phys. Conf.* 854 (No. 1) (2017, May), 012029 (IOP Publishing).
- [67] G.W. Qian, T. Ishihara, Numerical study of wind turbine wakes over escarpments by a modified delayed detached eddy simulation, *J. Wind Eng. Ind. Aerod.* 191 (2019) 41–53.
- [68] A.S. Dar, F. Porté-Agel, Three-dimensional wind-turbine wake characterization via tomographic particle-image velocimetry, *J. Phys. Conf.* 1618 (2020), 062045.
- [69] K.O. Emery, G.G. Kuhn, Sea cliffs: their processes, profiles, and classification, *Geol. Soc. Am. Bull.* 93 (7) (1982) 644–654.
- [70] T. Uchida, CFD Prediction of the airflow at a large-scale wind farm above a steep, three-dimensional escarpment, *Energy Power Eng.* 9 (13) (2017) 829–842.
- [71] M. Bastankhah, F. Porté-Agel, A new miniature wind turbine for wind tunnel experiments. Part i: design and performance, *Energies* 10 (7) (2017) 908.
- [72] R.B. Stull, *An Introduction to Boundary Layer Meteorology*, vol. 13, Springer Science, 2012.
- [73] M. Sherry, D.L. Jacono, J. Sheridan, An experimental investigation of the recirculation zone formed downstream of a forward facing step, *J. Wind Eng. Ind. Aerod.* 98 (12) (2010) 888–894.
- [74] R. Kilpatrick, H. Hangan, K. Siddiqui, D. Parvu, J. Lange, J. Mann, J. Berg, Effect of Reynolds number and inflow parameters on mean and turbulent flow over complex topography, *Wind Energy Sci.* 1 (2) (2016) 237–254.
- [75] International Electrotechnical Commission, International Standard, IEC 61400 Wind Turbines – Part 1 Design Requirements, IEC 61400-12:1998(E) (IEC 61400-1 Third edition 2005-08 edn), IEC, FDIS, Geneva, Switzerland, 2005, p. 92.
- [76] S. Shamsoddin, F. Porté-Agel, A model for the effect of pressure gradient on turbulent axisymmetric wakes, *J. Fluid Mech.* 837 (2018).
- [77] Y.T. Wu, F. Porté-Agel, Atmospheric turbulence effects on wind-turbine wakes: an LES study, *Energies* 5 (12) (2012) 5340–5362.
- [78] M. Bastankhah, F. Porté-Agel, A new miniature wind turbine for wind tunnel experiments. Part ii: wake structure and flow dynamics, *Energies* 10 (7) (2017) 923.
- [79] Y.T. Wu, F. Porté-Agel, Large-eddy simulation of wind-turbine wakes: evaluation of turbine parameterisations, *Boundary-Layer Meteorol.* 138 (3) (2011) 345–366.

- [80] P. Brugger, F.C. Fuertes, M. Vahidzadeh, C.D. Markfort, F. Porté-Agel, Characterization of wind turbine wakes with Nacelle-Mounted Doppler LiDARs and model validation in the presence of wind veer, *Rem. Sens.* 11 (19) (2019) 2247.
- [81] M. Bastankhah, F. Porté-Agel, Experimental and theoretical study of wind turbine wakes in yawed conditions, *J. Fluid Mech.* 806 (2016) 506–541.
- [82] M.F. Howland, J. Bossuyt, L.A. Martínez-Tossas, J. Meyers, C. Meneveau, Wake structure in actuator disk models of wind turbines in yaw under uniform inflow conditions, *J. Renew. Sustain. Energy* 8 (4) (2016), 043301.
- [83] D. Bastine, B. Witha, M. Wächter, J. Peinke, Towards a simplified dynamic wake model using pod analysis, *Energies* 8 (2) (2015) 895–920.